Determination and analysis of the constitutive parameters of temperature-dependent dislocation-density-based crystal plasticity models

Sedighiani, Karo; Traka, Konstantina; Roters, Franz; Raabe, Dierk; Sietsma, Jilt; Diehl, Martin

DOI
10.1016/j.mechmat.2021.104117

Publication date
2022

Document Version
Final published version

Published in
Mechanics of Materials

Citation (APA)
Sedighiani, K., Traka, K., Roters, F., Raabe, D., Sietsma, J., & Diehl, M. (2022). Determination and analysis of the constitutive parameters of temperature-dependent dislocation-density-based crystal plasticity models. *Mechanics of Materials*, *164*, Article 104117. https://doi.org/10.1016/j.mechmat.2021.104117

Mechanics of Materials 164 (2022) 104117

Contents lists available at ScienceDirect

Mechanics of Materials

journal homepage: www.elsevier.com/locate/mecmat

Research paper

Determination and analysis of the constitutive parameters of temperature-dependent dislocation-density-based crystal plasticity models

Karo Sedighiani [a,b,*], Konstantina Traka [a,b], Franz Roters [a], Dierk Raabe [a], Jilt Sietsma [b], Martin Diehl [a,c,d]

[a] Max-Planck-Institut für Eisenforschung, Max-Planck-Str. 1, 40237 Düsseldorf, Germany
[b] Department of Materials Science and Engineering, Delft University of Technology, Mekelweg 2, 2628 CD Delft, The Netherlands
[c] Department of Materials Engineering, KU Leuven, Kasteelpark Arenberg 44, 3001 Leuven, Belgium
[d] Department of Computer Science, KU Leuven, Celestijnenlaan 200 A, 3001 Leuven, Belgium

ARTICLE INFO

Dataset link: Experimental Data

Keywords:
Crystal plasticity
Dislocation density
Parameter identification
IF Steel
Compression test

ABSTRACT

Physics-based crystal plasticity models rely on certain statistical assumptions about the collective behavior of dislocation populations on one slip system and their interactions with the dislocations on the other slip systems. One main advantage of using such physics-based constitutive dislocation models in crystal plasticity kinematic frameworks is their suitability for predicting the mechanical behavior of polycrystals over a wide range of deformation temperatures and strain rates with the same physics-based parameter set. In this study, the ability of a widely used temperature-dependent dislocation-density-based crystal plasticity formulation to reproduce experimental results, with a main focus on the yield stress behavior, is investigated. First, the material parameters are identified from experimental macroscopic stress–strain curves using a computationally efficient optimization methodology that uses a genetic algorithm along with the response surface methodology. For this purpose, a systematic set of compression tests on interstitial free (IF) steel samples is performed at various temperatures and strain rates. Next, the influence of the individual parameters on the observed behavior is analyzed. Based on mutual interactions between various parameters, the ability to find a unique parameter set is discussed. This allows identifying shortcomings of the constitutive law and sketch ideas for possible improvements. Particular attention is directed toward identifying possibly redundant material parameters, narrowing the acceptable range of material parameters based on physical criteria, and modifying the crystal plasticity formulation numerically for high-temperature use.

1. Introduction

Crystal plasticity (CP) models are powerful and indispensable tools for modeling and understanding the relationship between the microstructure and the mechanical behavior of crystalline materials (Roters et al., 2010). In CP modeling, the deformation's kinetics is related to the physics of the material behavior through the constitutive law. Such constitutive law relies on internal state variables that constitute and track the deformation history. Various constitutive flow laws have been developed during the last few decades, e.g. phenomenological constitutive models (Voce, 1948; Hutchinson, 1976; Peirce et al., 1982; Becker, 1991) and physics-based constitutive models (Kocks et al., 1975; Nemat-Nasser et al., 1998; Arsenlis and Parks, 2002; Ma and Roters, 2004; Evers et al., 2002).

Phenomenological models use laws with fitted variables and are numerically cost-effective. While they incorporate the relevant features of plastic slip in metals via kinematic and kinetic assumptions, phenomenological models suffer from the drawback that they consider very limited physical information to define slip rates and the evolution of the internal variables. In other words, the internal variables are not directly related to physical quantities and, hence, their evolution laws are not related to physical processes, such as dislocation production, annihilation, interaction with other defects or thermal activation of specific dislocation processes. Therefore, any value of the constitutive parameters is deemed valid as long as the behavior of interest, such as the stress–strain curve, is predicted correctly, under the exact boundary and initial conditions where the parameters were fitted. This means, however, that there is no guarantee that the model correctly predicts the behavior for other loading conditions, e.g. strain rate and temperature, than the ones that have been used for fitting (Mandal et al., 2017).

* Corresponding author at: Department of Materials Science and Engineering, Delft University of Technology, Mekelweg 2, 2628 CD Delft, The Netherlands.
E-mail address: k.sedighiani@mpie.de (K. Sedighiani).

https://doi.org/10.1016/j.mechmat.2021.104117
Received 11 January 2021; Received in revised form 5 August 2021; Accepted 19 October 2021
Available online 6 November 2021

In contrast to phenomenological models, physics-based constitutive laws rely on physically-defined internal variables, e.g. typically dislocation densities, twin volume fractions, etc. (Roters et al., 2010). Dislocations are the most crucial internal variable type in the case of plasticity of materials with medium and high stacking fault energy as they are the carriers of the plastic deformation. In a physics-based crystal plasticity model, the plastic deformation is defined by the dislocation motion, and the hardening behavior is expressed in terms of generation, interaction, and annihilation of dislocations on different slip systems. Orowan (1934) related the plastic slip rate on a given slip system to the motion of dislocations through an average dislocation velocity. This dislocation motion is impeded by short-range and long-range barriers. The short-range barriers are those that can be overcome by thermal activation, while the long-range barriers are those which are too strong for thermal activation to be significant, such as the interaction between dislocations. At a finite temperature, thermal energy helps a dislocation to overcome short-range barriers by thermal activation, and the average dislocation velocity is determined by the probability of a successful jump from one obstacle to the next (Ono, 1968; Kocks et al., 1975; Regazzoni et al., 1987). Therefore, the average dislocation velocity is temperature-dependent. Kocks et al. (1975) decomposed the stress required for dislocation glide into an athermal component and a thermal component, and they related the probability of the successful jumps and the average dislocation velocity to the thermal stress.

The ideas of Kocks et al. (1975) form the basis for most temperature-dependent physics-based crystal plasticity models: Nemat-Nasser et al. (1998) suggested a dislocation-density-based model for face-centered cubic (fcc) and body-centered cubic (bcc) crystals which considers the effect of short-range and long-range barriers on the motion of dislocations. Voyiadjis and Abed (2005) proposed a constitutive model based on thermally activated dislocation glides, which takes into account the effect of the evolution of mobile and forest dislocation densities on the thermal and athermal parts of flow stress. Arsenlis and Parks (2002) implemented thermally activated dislocation-based constitutive laws into a crystal plasticity finite element (CPFE) simulation framework. Cheong and Busso (2004) developed a model in which the dislocations are discretized into edge and screw components with intrinsically different mobilities and dynamic recovery processes. Ma and Roters (2004), Ma et al. (2006a,b) developed a dislocation-density-based constitutive models for fcc and bcc crystals in which the geometrically necessary dislocation density is used in addition to the statistically stored dislocations in order to consider strain gradients and the microstructural size sensitivity. Evers et al. (2004b,a) developed a non-local crystal plasticity model that incorporates the interactions of various types of dislocation densities. Reuber et al. (2014) presented a model that explicitly accounts for the spatial redistribution of sign-polarized dislocation populations due to their motion. Monnet et al. (2013) proposed a dislocation-density-based crystal plasticity law for predicting the deformation behavior of bcc crystal at low- and high-temperature regimes. Alankar et al. (2014) presented a model for bcc crystals in which they considered the individual behavior of screw and edge dislocations. Cereceda et al. (2016) formulated and parametrized a velocity law for screw dislocations in bcc Tungsten based on atomistic simulations. Yuan et al. (2018, 2019, 2020) developed a model for single crystal plasticity which considers both dislocation glide and climb. Castelluccio and McDowell (2017) presented a cyclic crystal plasticity model by introducing a back stress formulation related to the mesoscale dislocation substructure. Luscher et al. (2017), Addessio et al. (2017) developed a dislocation-density-based model to investigate the deformation of metals under dynamic and shock-loading conditions. Keshavarz and Ghosh (2013, 2015), Ghosh et al. (2016), Keshavarz et al. (2016) proposed crystal plasticity constitutive models for modeling Ni-based superalloys in which the grain-scale response is obtained from the homogenization of the dislocation-density-based subgrain model. Wong et al. (2016) incorporated both transformation-induced plasticity and twinning-induced plasticity in a thermally activated dislocation-density-based crystal plasticity model. Patra and McDowell (2012, 2013, 2016), Li et al. (2014), Chakraborty and Bulent Biner (2016) developed crystal plasticity models for the inelastic deformation of irradiated bcc metals. Zhao et al. (2016, 2018) developed a coupled full-field model between fast Fourier transform-based crystal plasticity model and a phase-field recrystallization model to investigate the evolution of microstructural and micromechanical fields in polycrystals during dynamic recrystallization. These are only some examples of the diverse models developed in the past decades based on the temperature-dependent physics-based concept introduced by Kocks et al. (1975).

Furthermore, constitutive laws developed based on such thermally activated dislocation slip formulation are extensively used to investigate different deformation behavior such as the impact of hydrogen on the plastic deformation of metal under monotonic and cyclic loading (Castelluccio et al., 2018), the contribution of non-Schmid effects on the deformation behavior of Fe single crystal (Patra et al., 2014), the development of residual phase stresses due to processing in additively manufactured two-phase steel (Pokharel et al., 2019), the impact of crystallographic orientations on the evolution of misorientations and residual strains (Thool et al., 2020).

All such physics-based CP models have a large number of adjustable material parameters (Khan et al., 2015). Most of these constitutive parameters have a physical meaning, and the order of magnitude for them and most of their physics-defined upper and lower bounds are known (Ma and Roters, 2004; Khan et al., 2015). Physics-based models are, therefore, only correctly parametrized for a specific material under the two conditions that they predict the correct behavior (e.g. flow curves) *and* their parameters (e.g. the stacking fault energy) have the appropriate values. The advantage of a physically parametrized model is its *predictive* capability over a broad range of loading conditions using a single set of material parameters, i.e. all loading conditions for which the underlying physical processes do not change.

However, even though in physics-based CP models the order of magnitude for most of the parameters is known, a remaining obstacle for the routine use is posed by the complexity of calibrating its parameters for a desired material. In this study, a recently introduced methodology by Sedighiani et al. (2020), which uses a genetic algorithm along with the response surface methodology, is employed to determine the constitutive parameters of a temperature-dependent dislocation-density-based CP model introduced first by Ma and Roters (2004). A systematic series of compression tests were conducted at different deformation temperatures and strain rates on interstitial-free (IF) steel samples. The stress–strain curves from these experiments are used to determine the constitutive parameters. Furthermore, the uniqueness of the identified parameters is investigated. For this purpose, it is necessary first to understand the impact of the single-crystal parameters on the deformation behavior of polycrystals and second, to analyze the complex and non-linear interactions among the variables. The methodology introduced by Sedighiani et al. (2020) is also used for this task as it allows to quantitatively analyze the effect of different constitutive parameters and their interactions. Based on this analysis, the relevance and impact of the individual material parameters and their interactions are discussed. Moreover, the shortcomings of the constitutive law are addressed, and tighter bounds than those found in the literature are presented for selected parameters. The temperature-dependent motion of dislocations in the constitutive law used in this study has the same basis as the one proposed by Kocks et al. (1975). Therefore, most of the conclusions made in this study are applicable also to many other models that use the same concept, and this knowledge can help improve existing or newly developed constitutive laws.

This study is organized as follows. Section 2 summarizes the formulation of the crystal plasticity model employed in this work. Section 3 presents the experimental procedure and results of the compression tests conducted on IF steel at different temperatures and strain rates. This section is followed by a description of the simulation procedure and setup in Section 4. The identified material parameters and their

effects are presented in Section 5. The results are discussed in Section 6, which includes a discussion on the high-temperature instability of the CP model, acceptable physical ranges for some parameters, and the uniqueness of the identified material parameters. The main conclusions of this work are summarized in Section 7.

2. Physics-based crystal plasticity model

This section outlines the constitutive law of the CP model used in this study. The kinematics for elasto-plastic deformation is defined within the framework for finite deformation (Roters et al., 2010). The model is implemented in the open-source software DAMASK (Düsseldorf Advanced Material Simulation Kit), see (Roters et al., 2019; Diehl et al., 2020) for more detail.

2.1. Constitutive law

The shear rate on the slip system α, $\dot{\gamma}^\alpha$, is related to the (average) velocity of mobile dislocations, v^α, by the Orowan equation (Orowan, 1934):

$$\dot{\gamma}^\alpha = \rho^\alpha b v^\alpha, \tag{1}$$

where ρ^α is the mobile dislocation density of the slip system α, and b is the length of the Burgers vector for slip.

The dislocation velocity is mainly controlled by the distance between the short-range barriers and the average activation energy to overcome these barriers (Nemat-Nasser et al., 1998; Amirkhizi and Nemat-Nasser, 2007). The dislocation velocity is given as:

$$v^\alpha = \frac{l}{t_w + t_r}, \tag{2}$$

where l represents the average distance between the short-range barriers, t_w is the waiting time required to overcome a barrier, and t_r is the running time for a dislocation to move from one barrier to the next one. Based on the assumption that t_r is much smaller than t_w, the latter is often neglected (Amirkhizi and Nemat-Nasser, 2007). Following Kocks et al. (1975), the waiting time is estimated as:

$$t_w = \omega_0^{-1} \exp\left(\frac{\Delta G}{k_B T}\right), \tag{3}$$

where ΔG is the average activation energy to overcome the short-range barriers, ω_0 is the attempt frequency, T is the absolute temperature, and k_B is Boltzmann's constant. Using Eqs. (2) and (3), the dislocation glide velocity is calculated as:

$$v^\alpha = v_0 \exp\left(\frac{-\Delta G}{k_B T}\right), \tag{4}$$

where $v_0 = l\omega_0$ is the dislocation glide velocity pre-factor. Inserting Eq. (4) into Eq. (1), gives the shear rate of slip system α as:

$$\dot{\gamma}^\alpha = \rho^\alpha b v_0 \exp\left(\frac{-\Delta G}{k_B T}\right) \tag{5}$$

The stress dependence of $\dot{\gamma}^\alpha$ is due to the stress dependence of ΔG. ΔG can be formulated as:

$$\Delta G = \Delta F \left\{1 - \left[\frac{\tau_T^{*\alpha}}{\tau_0^*}\right]^p\right\}^q, \tag{6}$$

where ΔF is the total short-range barrier energy, i.e. the activation energy for glide in the absence of any applied stresses. p and q define the shape of the short-range barrier. For most barrier profiles, $0 < p \leq 1$ and $1 \leq q \leq 2$ (Kocks et al., 1975) holds. $\tau_T^{*\alpha}$ is the thermal component of the stress, which is calculated as:

$$\tau_T^{*\alpha} = \begin{cases} |\tau^\alpha| - \tau_\mu^\alpha & \text{for } |\tau^\alpha| > \tau_\mu^\alpha \\ 0 & \text{for } |\tau^\alpha| \leq \tau_\mu^\alpha \end{cases} \tag{7}$$

where τ^α is the total resolved shear stress on the slip system α, and τ_μ^α is the athermal component of the resolved shear stress which is given as:

$$\tau_\mu^\alpha = \mu b \left(\sum_{\alpha'=1}^{N_s} \xi_{\alpha\alpha'} (\rho^{\alpha'} + \rho_d^{\alpha'})\right)^{1/2}, \tag{8}$$

where ρ_d^α is the dislocation dipole density of the slip system α, $\xi_{\alpha\alpha'}$ is the interaction coefficient matrix between the different slip systems α and α', and μ is the shear modulus.

τ_0^* is the barrier strength, i.e. the stress needed to overcome short-range barriers without thermal assistance:

$$\tau_0^* = (|\tau^\alpha| - \tau_\mu^\alpha) \qquad \text{at} \quad T = 0 \text{ K}, \tag{9}$$

Combining Eqs. (5) and (6), the shear rate for slip system α is

$$\dot{\gamma}^\alpha = \rho^\alpha b v_0 \exp\left(\frac{-\Delta F}{k_B T}\left\{1 - \left[\frac{\tau_T^{*\alpha}}{\tau_0^*}\right]^p\right\}^q\right) \text{sign}(\tau^\alpha), \tag{10}$$

Dislocation density evolution

The evolution rate of the mobile dislocation density is given as (Roters et al., 2019; Blum and Eisenlohr, 2009):

$$\dot{\rho}^\alpha = \frac{|\dot{\gamma}^\alpha|}{b\Lambda^\alpha} - \frac{2d_{\text{dipole}}^\alpha}{b}\rho^\alpha|\dot{\gamma}^\alpha|, \tag{11}$$

and the evolution rate of the dislocation dipole density is defined as (Blum and Eisenlohr, 2009):

$$\dot{\rho}_d^\alpha = \frac{2(d_{\text{dipole}}^\alpha - d_{\text{anni}}^\alpha)}{bb}\rho^\alpha|\dot{\gamma}^\alpha| - \frac{2d_{\text{anni}}^\alpha}{b}\rho_d^\alpha|\dot{\gamma}^\alpha|. \tag{12}$$

The dislocation multiplication rate, see the first term in Eq. (11), is determined by the dislocation mean free path Λ^α (Roters et al., 2019):

$$\frac{1}{\Lambda^\alpha} = \frac{1}{d_g} + \frac{1}{\lambda^\alpha}, \tag{13}$$

where d_g is the effective grain size, and

$$\frac{1}{\lambda^\alpha} = \frac{1}{C_\lambda}\left(\sum_{\alpha'=1}^{N_s} g_{\alpha\alpha'}(\rho^{\alpha'} + \rho_d^{\alpha'})\right)^{1/2}, \tag{14}$$

where C_λ is a coefficient that determines the number of dislocations passed by a dislocation before forest dislocations trap it. $g_{\alpha\alpha'}$ are coefficients that account for the interaction between dislocations on different slip systems.

The mobile dislocation density decreases due to annihilation and dipole formation, as described in the second term of Eq. (11). Dislocation annihilation occurs when two mobile dislocations of opposite signs meet each other within the area of $2d_{\text{anni}}^\alpha v^\alpha \mathrm{d}t$ during a time increment of $\mathrm{d}t$. d_{anni}^α represents a critical distance for annihilation of two mobile dislocations of opposite sign. Commonly, a dislocation annihilation coefficient, C_{anni}, is introduced to express d_{anni}^α in multiples of the Burgers vector: $d_{\text{anni}}^\alpha = C_{\text{anni}} b$. The annihilation term in Eq. (11) is calculated based on the assumption that the system contains equal numbers of positive and negative dislocations.

The dipole formation also decreases the mobile dislocation density. A dipole is formed if two mobile dislocations with opposite sign have a distance above d_{anni}^α but less than the critical radius for dipole formation, d_{dipole}^α, see the first term in Eq. (12). The critical distance for dipole formation is defined as:

$$d_{\text{dipole}}^\alpha = \frac{\mu}{16\pi|\tau^\alpha|} b, \tag{15}$$

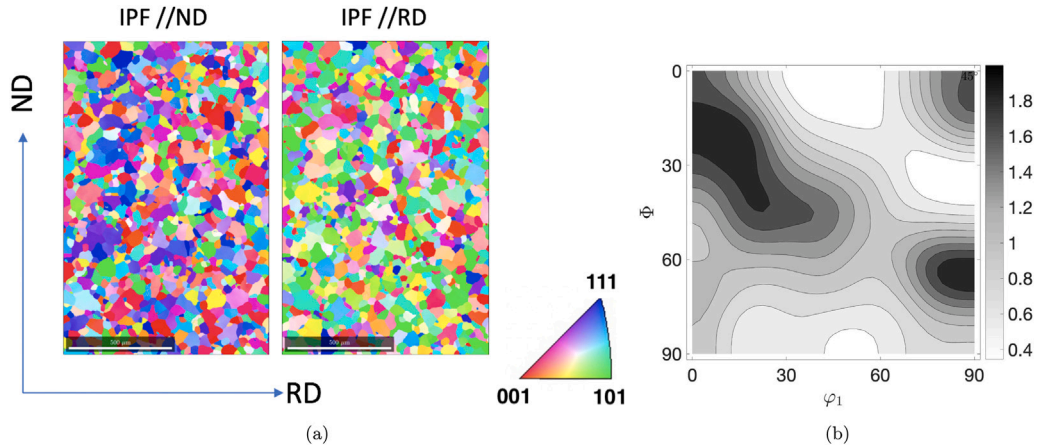

Fig. 1. (a) Electron backscatter diffraction inverse pole figure map of the hot rolled IF-steel measured across the thickness (ND) perpendicular to the rolling direction (RD), and (b) $\varphi_2 = 45°$ ODF section of the as-received hot-rolled IF steel (Sedighiani et al., 2020).

Table 1
The chemical composition of the IF steel considered in this study.

Element	C	Mn	S	Ti	N	Al	Cr	Fe
wt. (%)	0.002	0.095	0.006	0.045	0.002	0.05	0.02	Balance

3. Experiments

3.1. Material

The material used in the present study is an IF steel with chemical composition as given in Table 1. The initial microstructure and crystallographic texture of the material were measured across the thickness (ND) perpendicular to the rolling direction (RD) using electron backscatter diffraction (EBSD). Standard metallographic techniques were used to prepare the specimens for characterization. Analysis of the EBSD data was performed using the TSL OIM software. The grain structure is almost equiaxed, and the material exhibits a mild texture, see Fig. 1.

3.2. Compression testing

The uniaxial compression tests were performed in a Bähr DIL 805A/D deformation dilatometer. Cylindrical specimens with a diameter of 3 mm and a height of 6 mm were extracted by wire electrical discharge machining from the as-delivered hot-rolled sheet along the rolling direction. The temperature of the specimens was measured during the heating and deformation by means of a thermocouple attached to the surface of the specimen. The specimens were heated to the deformation temperatures with a heating rate of $50\,\mathrm{K\,s^{-1}}$ and then held at the deformation temperature for 2 s before applying the deformation.

Specimens were deformed to a logarithmic strain of about 0.65. However, for a few cases of low temperatures and high strain rates, the applied strain was limited to 0.4 or 0.5 to prevent exceeding the load limit of the machine. Nine different deformation temperatures, namely 323, 373, 473, 573, 673, 773, 873, 973, and 1073 K, and three different strain rates, namely 0.01, 0.1, and 1.0 $\mathrm{s^{-1}}$, were used in compression tests. All tests were performed at isothermal loading conditions. However, for low temperature and high strain rate cases of $(T, \dot{\varepsilon}) = (323\ \mathrm{K}, 1.0\ \mathrm{s^{-1}})$, $(373\ \mathrm{K}, 1.0\ \mathrm{s^{-1}})$, and $(473\ \mathrm{K}, 1.0\ \mathrm{s^{-1}})$, a temperature rise of 31, 26, and 11 K, respectively, was observed. For all other experiments, the temperature rise during deformation was negligible.

The equivalent true stress–logarithmic strain curves obtained from the compression tests at different temperatures and strain rates are shown in Fig. 2. Generally, it can be seen that the hardening rate decreases with an increase in deformation temperature for a given strain rate, and it increases with an increase in strain rate for a fixed deformation temperature. In this work, all comparisons between simulated and the experimental data are performed using the equivalent true stress and equivalent logarithmic strain. For the sake of brevity, they will be referred to as stress and strain, respectively, in the remainder of this study.

Fig. 3 shows the variation of yield stress with deformation temperature at different strain rates. It is obvious that the influence of deformation temperature and strain rate on the yield stress is significant for the tested conditions. For a given strain rate, a decrease in yield stress can be seen with an increase in temperature. In contrast, the yield stress increases with an increase in strain rate for a given deformation temperature. However, the rate of change in the yield stress is considerably dependent on the deformation temperature and strain rate. At low temperatures, the yield stress is highly temperature and strain rate sensitive. The sensitivity to a change in deformation temperature or strain rate decreases by increasing the deformation temperature. An intermediate regime is observed at which the sensitivity to a change in deformation temperature or strain rate is minimal. After this transition regime, the dependency of the yield stress to temperature and strain rates increases again.

4. Simulations

A Fast Fourier Transform (FFT)-based spectral solver implemented in DAMASK (Eisenlohr et al., 2013; Shanthraj et al., 2015, 2019) is used to conduct CP simulations using the constitutive law outlined in Section 2. It is assumed that the slip occurs on 24 slip systems: 12 slip systems of <111>{110} and 12 slip systems of <111>{112}. The representative volume element (RVE) is made of 512 grains, as shown in Fig. 4(a). A grid with dimension 8 × 8 × 8 was used, i.e. each grain is represented by one voxel. The texture and the crystallographic orientations of the grains were assigned according to the EBSD map of the undeformed sample using the approach presented in Eisenlohr and Roters (2008). Fig. 4(b) shows the $\varphi_2 = 45°$ ODF section of the RVE. Periodic boundary conditions hold on this RVE which was subjected to uniaxial compression up to around 0.4 strain.

Table 2
Ranges of the adjustable model parameters used in the optimization.

Variable	Description	Units	Range
ρ_0^α	Initial dislocation density	m/m^3	$[10^{11}, 10^{13}]$
$v_0 = l\omega_0$	Dislocation glide velocity pre-factor	m/s	$[10^2, 10^4]$
ΔF	Activation energy for dislocation glide	J	$[1.3, 2.5] \times 10^{-19}$
p	p-exponent in glide velocity	–	[0.25, 0.7]
q	q-exponent in glide velocity	–	[1.2, 1.85]
τ_0^*	Short-range barriers strength at 0 K	MPa	[300, 600]
C_λ	Parameter controlling dislocation mean free path	–	[10, 50]
C_{anni}	Coefficient for dislocation annihilation	–	[2, 15]

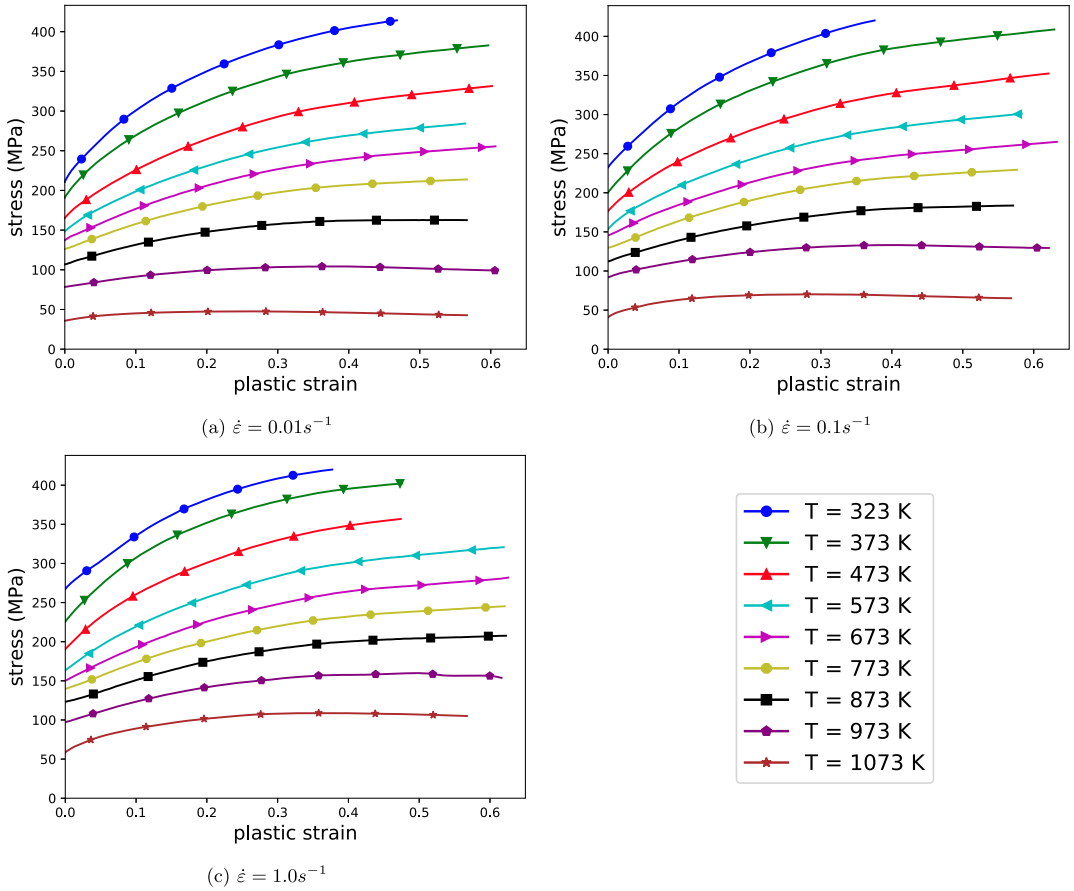

Fig. 2. Equivalent true stress–logarithmic strain curves for IF steel deformed by compression at various temperatures at strain rates of (a) 0.01 s^{-1}, (b) 0.1 s^{-1}, and (c) 1.0 s^{-1}.

4.1. Adjustable model parameters

Table 2 lists the ranges of the adjustable model parameters used to build the off-line database for the response surface methodology, see Sedighiani et al. (2020) for more information. These ranges are selected based on the physical interpretation of the parameters and the values reported in the literature. However, the ranges provided in the literature for p and q are considered as too wide. Therefore, new ranges are introduced for them as elaborated in more detail later (Section 6.2).

4.2. Fixed model parameters

In this study, some of the parameters are considered to be known and fixed. These parameters will not be studied in the optimization procedure. The elastic coefficients are considered to be temperature-dependent, and they are taken from Dever (1972), Adams et al. (2006). The dislocation interaction coefficients are also taken as an average value for iron from Madec and Kubin (2017), see Table 3. The Burgers vector is also a known material constant and equals 0.248 nm.

Table 3
Coefficients of interaction between different slip systems.

Self	Coplanar	Collinear	Orthogonal	Glissile	Sessile
0.1	0.1	0.72	0.053	0.137	0.073

5. Results

5.1. Optimized parameters

The values selected for material parameters strongly influence a crystal plasticity model's ability to correctly predict a specific material's deformation behavior. Therefore, a prerequisite for utilizing any constitutive models is determining a proper set of material parameters. Theoretically, most of the material parameters for a physics-based crystal plasticity model can be determined directly from single-crystal experiments (Bertin et al., 2016; Raabe et al., 2001). However, since engineering materials are usually only available as polycrystals after synthesis, homogenization, and processing, it is more convenient to

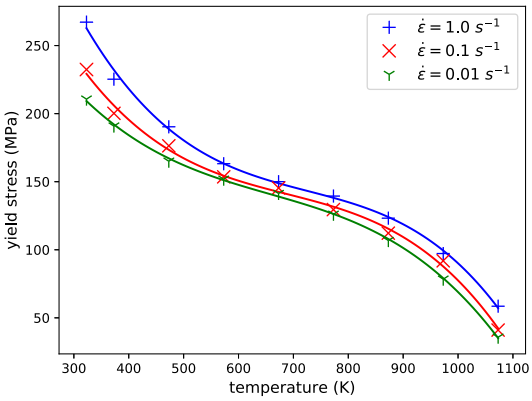

Fig. 3. Variation of yield stress with temperature for different strain rates. The solid lines are third-order regression lines.

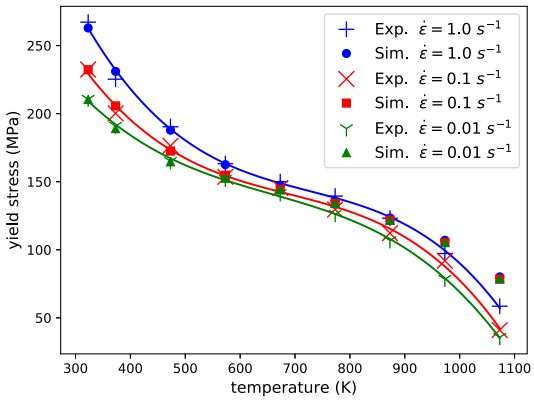

Fig. 5. Predicted yield stress versus temperature for optimized parameters as compared with experimental data. The solid lines are third-order regression lines for the experimental data. The crystal plasticity model is capable of predicting the yield stress over a wide range of temperatures and strain rates using a single set of material parameters. However, the model fails to correctly predict the material response at temperatures above 800 K. This indicates that the CP model does not include some physical effects occurring at elevated temperatures.

identify the material parameters from experimental macroscopic tests such as stress–strain data. Recently, Sedighiani et al. (2020) introduced a computationally efficient approach to identify and quantify the material parameters from macroscopic stress–strain curves. This methodology is used here to determine the material parameters for IF steel. The suggested methodology uses a genetic algorithm, together with the response surface methodology. The methodology is also employed to quantitatively and systematically analyze the relatively complex dislocation-density-based CP model. Appendix A provides a brief summary of the methodology which is presented in detail in Sedighiani et al. (2020).

Table 4 lists the optimized constitutive parameters obtained for IF steel. This set of parameters can be used to capture the temperature and strain rate sensitivity of the plastic deformation for a wide range of temperatures and strain rates. CP simulations are performed using this single set of parameters, and the results obtained for yield stress are discussed in Section 5.1.1. In addition, the uniqueness and dependency of these parameters are discussed in Section 6.3. It should be noted that the values of C_λ and C_{anni} are dependent on the other recovery mechanisms employed in the crystal plasticity model. However, the yield stress behavior is independent of these two parameters, and their values do not affect the determination of the rest of the parameters, see Section 5.2.1 for more information. Therefore, in this work, these two parameters are not further discussed.

5.1.1. Yield stress prediction

The yield stress in dependence of temperature predicted with the optimized parameters is shown in Fig. 5. The experimental data is given for comparison. It can be seen that the crystal plasticity model is capable of predicting the yield stress over a wide range of temperatures and strain rates. Moreover, the model is able to capture the rate sensitivity at different temperatures and vice versa. The maximum error observed for temperatures lower than 773 K is approximately 5.7 MPa, which is for the loading condition of $T = 373$ K and $\dot{\varepsilon}_p = 1.0\ \text{s}^{-1}$. However, the model fails to correctly predict the material response at temperatures above 800 K. Around this point, there is a second pronounced drop in the experimental data, while the simulations predict only a much smaller decrease.

To investigate the observed discrepancy between the simulation results and the experimental data, Eq. (10) is rewritten for the resolved shear stress as a function of shear rate and temperature:

$$\tau^\alpha = \tau_\mu^\alpha + \tau_T^{*\alpha} = \tau_\mu^\alpha + \tau_0^* \left[1 - \left(-\frac{k_B T \ln\left(\frac{|\dot{\gamma}^\alpha|}{\rho^\alpha b v_0 \omega_0}\right)}{\Delta F} \right)^{\frac{1}{q}} \right]^{\frac{1}{p}}, \tag{16}$$

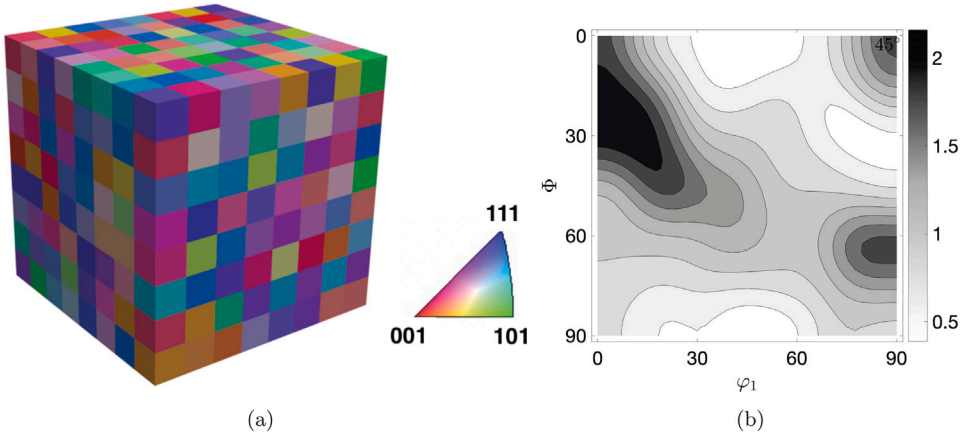

Fig. 4. (a) Voxel representation of the RVE used in the CP simulations. The RVE is made of 512 grains and each grains is represented by one voxel. The coloring displays the Inverse Pole Figure (IPF) color map parallel to the loading (vertical) direction. (b) $\varphi_2 = 45°$ ODF section of the RVE. (For interpretation of the references to color in this figure legend, the reader is referred to the web version of this article.)

Table 4
Optimized constitutive parameters for IF steel.

ρ_0^α(m^{-2})	υ_0 (ms^{-1})	ΔF (J)	τ_0^* (MPa)	p	q	C_λ	C_{anni}
2.81×10^{12}	1.4×10^{3}	1.57×10^{-19}	454	0.325	1.55	23.3	7.4

Table 5
The initial dislocation density needed to reproduce the experiential data for three exemplar loading conditions.

Loading conditions	(973 K, 0.1 s^{-1})	(1073 K, 0.01 s^{-1})	(1073 K, 1.0 s^{-1})
ρ_0^α (m/m^3)	2.14×10^{12}	5.85×10^{11}	1.50×10^{12}

Table 6
The required reduction in the dislocation interaction coefficients to reproduce the experimental data for three exemplar loading conditions.

Loading conditions	(973 K, 0.1 s^{-1})	(1073 K, 0.01 s^{-1})	(1073 K, 1.0 s^{-1})
Reduction (%)	25%	79%	47%

The derivative with respect to temperature of Eq. (16) can be calculated as:

$$\frac{\mathrm{d}\tau^\alpha}{\mathrm{d}T} = -\frac{\tau_0^*\left(-\frac{k_B T \ln(\frac{|\dot\gamma^\alpha|}{\rho^\alpha b\upsilon_0\omega_0})}{\Delta F}\right)^{\frac{1}{q}}\left[1-\left(-\frac{k_B T \ln(\frac{|\dot\gamma^\alpha|}{\rho^\alpha b\upsilon_0\omega_0})}{\Delta F}\right)^{\frac{1}{q}}\right]^{-1+\frac{1}{p}}}{p\,q\,T}, \tag{17}$$

These equations indicate that the thermal stress smoothly decreases for an increase in temperature, see also Fig. 7. However, based on Eq. (17), the rate of decrease in thermal stress decreases with an increase in temperature until it becomes zero at a critical temperature, T_c. After this point, the thermal stress component vanishes, and the athermal component solely determines the resolved shear stress, see Section 6.1. Therefore, the CP model predicts a smooth decrease of the flow stress until a plateau at T_c is reached. Consequently, the second drop in the yield stress cannot be predicted using this type of thermally activated constitutive law. It should be noted that the ongoing decrease of the yield stress seen in the simulation results is only due to the dependency of the athermal stress to temperature through the temperature dependency of the shear modulus. Consequently, this decrease is independent of the applied strain rate.

The experimentally observed drop of the yield stress for higher temperatures suggests the activation of a new mechanism at high temperatures. One possible explanation for this second drop is climb-based recovery during the heating period prior to deformation. The reduced initial dislocation densities to match the experimental data are listed in Table 5 for three exemplar loading conditions. The data show that a considerable amount of recovery is required before the onset of the plastic deformation to reproduce the experimental data. However, the specimens were machined from an as-delivered hot-rolled sheet and consequently, the EBSD data shows no in-grain misorientation patterns. Moreover, the high heating rate, 50 K s^{-1}, used to heat up the samples prior to deformation kept the time at elevated temperatures short. Therefore, significant recovery does not seem a plausible explanation for the decrease of the yield stress for testing temperatures above approximately 800 K.

A second possibility to explain the second drop is a dependency of the dislocation interaction coefficients, $\xi_{\alpha\alpha'}$, on the temperature. However, these interactions are typically considered as too strong for thermal activation to be significant. Nevertheless, Table 6 lists the required reduction in the dislocation interaction coefficients to reproduce the experimental data under the assumption of a constant ratio for all interactions. It can be seen that a significant reduction in the dislocation interaction coefficients is required. Therefore, the temperature dependency of the dislocation interaction coefficient would be too high to be physically plausible.

A third possibility to explain the second drop can be attributed to the way Eq. (10) is derived. In this form of a thermally activated constitutive law, the short-range barriers are defined in an average sense using an average barrier's strength τ_0^* and average activation energy for glide ΔF. The average shape of the barriers is defined by p and q. However, short-range barriers may have different characteristics and physical meaning, and it may not be possible to present all types of barriers collectively as one average set. Therefore, one suggestion to solve this issue is to estimate the dislocation velocity using two or more different classes of short range obstacles. A promising approach for novel CP constitutive models targeting deformations at high temperature, therefore, is the consideration of a temperature dependence of obstacles. However, evaluating such new and more complex approach is beyond the scope of this paper.

Finally, as a fourth possibility, the second drop of the yield stress observed at high temperatures can be attributed to the use of an isotropic effective shear modulus when calculating the effect of dislocation interactions in Eq. (8). Voigt's (Voigt, 1889) and Reuss's (Reuss, 1929) assumptions are the two approaches for calculating the equivalent shear modulus which predict the upper and lower bounds of the effective shear modulus (Hill, 1952), respectively. In this study, the former assumption is used. However, since for ferritic steels the anisotropy ratio $2C_{44}/(C_{11}-C_{12})$ rises from approximately 2.4 at 300 K to approximately 7.4 at 1173 K, the assumption of an isotropic equivalent shear modulus might be inappropriate for elevated temperatures. At least at the level of individual dislocations, it is well-established that the elastic anisotropy has strong effects on the yield behavior (Fitzgerald and Dudarev, 2008; Fitzgerald, 2010; Aubry et al., 2011) and high elastic anisotropy may result in a pronounced softening irrespective of the mean shear modulus (Fitzgerald, 2010). It remains an open question how this knowledge from small scale investigations can be used to improve the mean field approximations used in continuum scale CP formulations.

5.2. Constitutive parameters effects and their interaction

Fig. 6 shows the main effects and the interaction effects of the adjustable material parameters on the yield stress. A main effect shows how a change in an explanatory variable affects the response variable, ignoring all other explanatory variables' effects. An interaction effect indicates how an explanatory variable's effect may depend on the other explanatory variables' level. Eq. (A.3) is used to calculate the magnitudes of the effects and the interaction effects. It is clear that the most significant positive main effects are p, τ_0^*, ΔF, and ρ_0^α, and the most significant negative main effect are q, and υ_0. Additionally, the interactions between some of the material parameters are significant, e.g. the interaction effect between p and τ_0^*. The results also reveal that both the temperature and the strain rate sensitivities are controlled essentially by the material parameters that define the barrier, i.e. τ_0^*, ΔF, p, and q. In this study, we only show effects with an absolute magnitude larger than 30 % of the most significant effect's absolute magnitude. However, based on the ANOVA (analysis of variance) output (Doncaster and Davey, 2007), there are many more statistically significant effects than those shown in the figures. For a full discussion on the effect analysis see Sedighiani et al. (2020)

5.2.1. Grouping the parameters

The yield stress is controlled mainly by p, τ_0^*, ΔF, ρ_0^α, q, and υ_0, while the hardening behavior depends mainly on C_{anni} and C_λ, see Sedighiani et al. (2020) for detailed discussion. In addition, there is no significant interaction between C_{anni} and C_λ on the one hand and p, τ_0^*, ΔF, ρ_0^α,

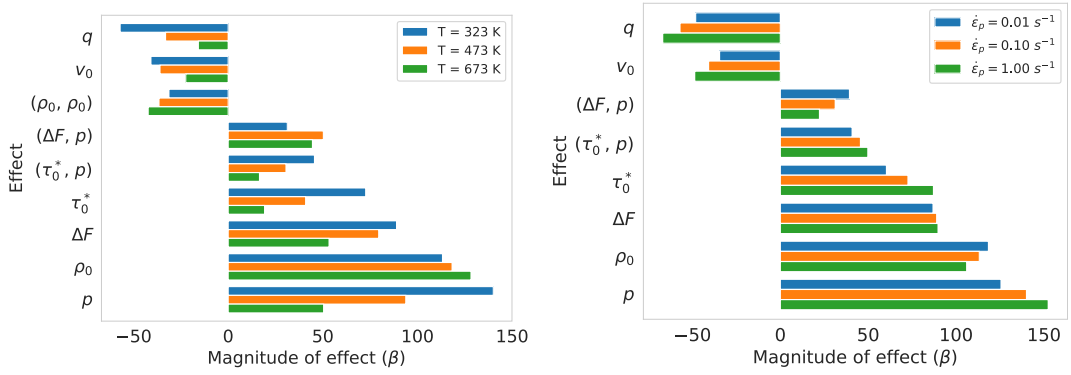

(a) $\dot{\varepsilon}_p = 0.1s^{-1}$ (b) $T = 323K$

Fig. 6. The main effects and interactions effects for the yield stress (a) for $\dot{\varepsilon} = 0.1s^{-1}$ at varying temperatures, (b) for $T = 323$ K at varying strain rates. The effects are in MPa, and their magnitudes are calculated using Eq. (A.3). For the definition of the material parameters see Table 2.

q, and v_0 on the other hand. This opens the possibility of splitting the material parameters into two groups for the response surface methodology (RSM) analysis and determining parameters in these groups independently. For instance, using experimental data for yield stress alone is sufficient for accurate identification of p, τ_0^*, ΔF, ρ_0^α, q, and v_0. Additionally, grouping the parameters substantially decreases the number of simulations needed to build the off-line database and results in a smaller error in the response predicted by the RSM (Sedighiani et al., 2020). In the following, the influence of the parameters that determine the yield strength, i.e. p, τ_0^*, ΔF, ρ^α, q, and v_0 is discussed.

6. Discussion

6.1. Importance of running time for high-temperature applications

The optimization methodology introduced in this study explores different combinations of material parameters at different loading conditions to find a set of parameters that reproduces all experimental results. Consequently, its success depends on the stability of the CP model within the whole parameter space. However, no converge was observed for certain parameter combinations at elevated temperatures. In this subsection, the reason for this instability and an approach to overcome this issue are discussed.

The constitutive law is based on the assumption that dislocation motion is impeded by short-range and long-range barriers. The short-range barriers are those barriers that can be overcome by thermal activation, while the long-range barriers are essentially independent of temperature since they are too strong for thermal activation to be significant. Therefore, the resolved shear stress consists of a thermal component, $\tau_T^{*\alpha}$, and an athermal component, τ_μ^α. The thermal component is the main reason for the temperature and strain rate sensitivity of the flow stress. The athermal component is temperature-dependent only through the temperature dependency of the shear modulus, see Eq. (8).

An increase in the deformation temperature or a decrease in the applied strain rate increases the probability of thermal activation, which results in a reduction in the flow stress. However, there is a critical temperature T_c, above which there is sufficient thermal energy to overcome the short-range barriers by thermal activation alone, i.e. $\tau_T^{*\alpha} = 0$. The critical temperature can be calculated as:

$$T_c = -\frac{\Delta F}{k_B \log[\frac{|\dot{\gamma}^\alpha|}{\rho^\alpha b v_0}]} \tag{18}$$

For temperatures above the critical temperature, the shear rate formulation reduces to:

$$\dot{\gamma}^\alpha = \rho^\alpha b v_0 \exp\left(\frac{-\Delta F}{k_B T}\right) \quad \text{for} \quad T \geqslant T_c \tag{19}$$

At the starting point of the plastic deformation, ρ^α can be considered as a constant parameter and equal to ρ_0^α for all samples. Therefore, all parameters in this equation are constant except T. Hence, for $T \geqslant T_c$, the shear rate is related to temperature only and does not depend on the effective applied stress. This results in numerical instabilities and convergence cannot be achieved at temperatures close to and above the critical temperature.

To understand why the original formulation is numerically unstable at high temperatures, it should be recalled that the dislocation velocity is controlled by the waiting time and running time, see Eq. (2). It is generally assumed that the running time is much smaller than the waiting time, and, hence, its effect is negligible. However, at temperatures close to or above the critical temperature, this assumption is no longer valid and the running time is comparable to or even higher than the waiting time. Therefore, it cannot be neglected. The running velocity of a dislocation follows a viscous flow law (Hansen et al., 2013; Cereceda et al., 2016; Reuber et al., 2014):

$$v_r^\alpha = \frac{\tau_T^{*\alpha} b}{B}, \tag{20}$$

Substituting this equation into Eq. (2) give the effective velocity as:

$$v^\alpha = \frac{l}{t_w + t_r} = \frac{1}{\frac{t_w}{l} + \frac{t_r}{l}} = \frac{1}{\frac{1}{v_b^\alpha} + \frac{1}{v_r^\alpha}}, \tag{21}$$

where $v_b^\alpha = t_w/l$ is the same velocity as presented earlier in Eq. (4).

For temperatures much lower than the critical temperatures, $v_b^\alpha \ll v_r^\alpha$ holds, and the original formulation is approximately recovered. However, with increasing temperature the running time will become more important until it finally fully determines the velocity. Therefore, numerical instabilities described in Eq. (19) are avoided and a physically sound behavior is achieved even for higher temperatures. This allows to find suitable parameter combinations from the whole parameter space, which does not contain "forbidden regions" of numerical instabilities (cf. Sections 6.2 and 6.3.2).

6.2. Limiting material parameters p and q based on physical criteria

The profile of the barrier is controlled via parameters p and q, which are usually seen as free parameters with $0 < p \leq 1$ and $1 \leq q \leq 2$ (Kocks et al., 1975). However, these limits present only the extreme cases for which Eq. (16) is mathematically valid. In this section, the effect of these two parameters on the thermal stress is discussed and an approach is presented for determining (more narrow) physical limits.

The parameters p, q, ΔF, and τ_0^* together define the relation between the activation energy for dislocation glide, ΔG, and the thermal component of the stress, $\tau_T^{*\alpha}$. However, the development of thermal

stress with temperature is affected differently by these parameters. ΔF is a coefficient for the temperature-dependent ratio inside the exponential term, and it linearly affects this ratio. As a result, the critical temperature T_c is linearly dependent on ΔF, while it is independent of the other three barrier parameters, see Eq. (18). The stress needed to overcome the barrier at 0 K is solely defined by the barrier strength τ_0^*. The curvature between 0 K and T_c, is defined by p and q. Although both of the parameters have a significant effect on the curvature for all temperatures between these two points, the effect of p and q is more pronounced at high and low temperatures, respectively (Fig. 7).

The limits proposed in the literature for p and q are defined based on mathematical arguments, and they describe the experimental observations only qualitatively. For $p > 1.0$ or $q < 1.0$, the sign of the curvature in the thermal stress versus temperature curve is reversed in comparison to the experimentally observed behavior. For $p \leq 0$ the resolved shear stress becomes larger than the barrier strength. To our knowledge, there is no such argument why q should be strictly smaller than 2. One reason, however, can be the intense effect of a large q at very low temperatures, i.e. a large q results in a significant drop in the thermal stress with a small increase in temperature. To prevent such an extreme condition, having an upper bound for q seems physically reasonable.

As outlined, the advised limits for p and q except the upper bound for q only ensure that the general shape of the curve is qualitatively reasonable. However, unwanted behavior is already observed when choosing values in the vicinity of the limits. For instance, a small p results in an almost constant τ^* over a vast range of temperatures, see the red dashed line in Fig. 7. Although a wide temperature-insensitive regime has been observed for some materials, modeling this phenomenon by setting p to small values results in an unphysical barrier profile: A small p requires a higher value for ΔF which in turn increases T_c beyond reasonable values. It is physically more meaningful to attribute the temperature insensitivity to the critical temperature and the energy needed to overcome the barrier. As mentioned earlier, the thermal stress vanishes for temperatures larger than the critical temperature, and a temperature-insentitive behavior is naturally achieved.

Now the question arises whether there is a physics-based limit for p and q. There may be no exact answer to this question because of two main reasons: Firstly, these two parameters are introduced into the equations in a phenomenological way, and they are not derived based on any obstacle profiles. Secondly, there is a strong correlation between these two parameters, which results in a dependency of the limiting bounds to the value of the other parameter. For example, a range for p may be reasonable at a specific q, while it is not reasonable for another q.

Although no strict physics-based limit can be provided for p and q, it is still possible to limit these two parameters based on physical criteria. Combining Eqs. (10) and (19) gives:

$$\left(\frac{\tau_T^{*\alpha}}{\tau_0^*}\right)^p = 1 - \left(\frac{T}{T_c}\right)^{\frac{1}{q}} \tag{22}$$

A lower bound for p can be determined by setting a limit for the degree of flatness of the thermal stress before T_c. In other words, by setting a reasonable minimum increase in the stress ratio at a specific temperature ratio, a lower bound for p can be estimated. For example, by assuming the minimum required stress ratio of $\tau_T^{*\alpha}/\tau_0^* = 0.001$ at $T/T_c = 0.8$, the lower limit for p is approximately 0.25 when $q = 1$. The choice of $p = 0.25$ already results in an extremely wide temperature-insensitive regime below the critical temperature.

A literature survey shows, however, that small values for p, such as 0.1, have been frequently identified to match experimental data, e.g. Arsenlis and Parks (2002), Alankar et al. (2009), Ha et al. (2017), Khan et al. (2015). The reason for the frequently reported small p could be related to the numerical difficulties at temperatures close to or above the critical temperature, see Section 6.1. A small p has been used to increase the critical temperature, and consequently to postpone the numerical instability. However, the numerical difficulties can be overcome using the alternative formulation presented for dislocation velocity in Section 6.1, making artificially high critical temperatures unnecessary.

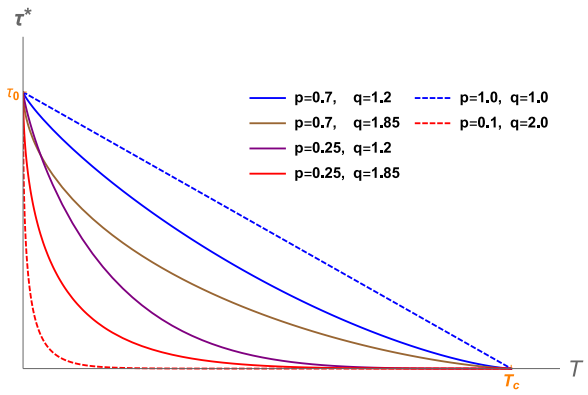

Fig. 7. Thermal stress versus temperature for different combinations of p and q. The usual limits for p and q are $0 < p \leq 1$ and $1 \leq q \leq 2$. Setting $p = 1$ and $q = 1$, the blue dashed line, results in a linear relationship between thermal stress and temperature, which corresponds to a physically unreasonable rectangular profile for the barrier and a non-smooth transition at the critical temperature. A small p, such as $p = 0.1$, results in a physically unacceptable flat curve for a vast range of temperatures below T_c, and it indirectly shifts the critical temperature, see the red dashed line. Although no strict physics-based limit can be provided for p and q, it is still possible to limit them in a physically measurable way using the slope of the curve at 0 K and T_c. The solid lines show the resulting curves for different combinations of p and $q$using the limits calculated in this study. (For interpretation of the references to color in this figure legend, the reader is referred to the web version of this article.)

Eq. (22) can also be used to estimate an upper bound for q. For example, by assuming a maximum acceptable drop of 5 % in the stress ratio, i.e. $\tau_T^{*\alpha}/\tau_0^* = 0.95$, at $T/T_c = 0.001$, the upper limit of $q \approx 1.85$ is achieved when $p = 0.5$. Even $q = 1.85$ results in a relatively sharp drop in the thermal stress for a very small increase in temperature. Therefore, it seems physically reasonable to use $q < 1.85$ when p is close to 0.5. It should be noted that the upper bound of q is strongly dependent on p, and an higher bound for q can be reasonable for a large p.

Setting $p = 1$ and $q = 1$ results in a linear relationship between thermal stress and temperature as shown in Fig. 7, which corresponds to a rectangular profile for the barrier. Such a barrier profile results in a non-smooth transition at the critical temperature. Therefore, one may consider an upper bound around 0.7–0.8 for p to have a smoother transition at the critical temperature. The same argument may be used for q, and one may consider a lower bound of 1.2 for q. Fig. 7 shows thermal stress versus temperature for the suggested bounds.

It should be noted that the mentioned ranges for p and q still include extreme combinations which may result in unphysical behaviors, see the red solid line in Fig. 7. This is especially true for regimes where p approaches the lower bound, and q approaches the upper bound.

6.3. Uniqueness and relevance of parameters

In this section, the uniqueness of the parameters obtained as the optimal solution by the RSM-GA approach is discussed. For the sake of convenience, the parameters are categorized into two groups: The first group includes v_0 and ρ_0^α. These two parameters characterize the most relevant features of the dislocation network for plastic deformation, i.e. the dislocation density and the distribution of dislocation segment lengths. They have a linear relationship with the shear rate, see Eq. (10). The second group includes those parameters that define the short-range barrier, i.e. p, q, τ_0^*, and ΔF. These parameters appear in the exponential part of the shear rate formulation.

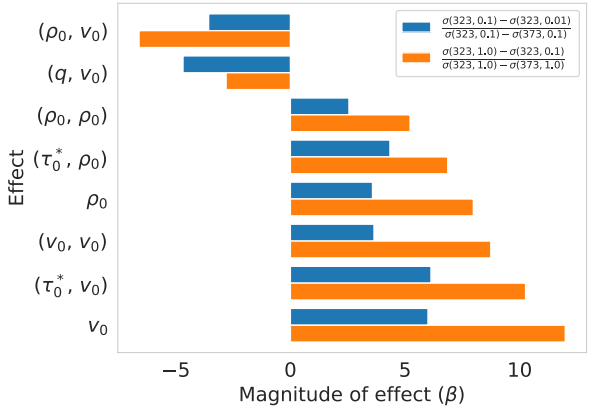

Fig. 8. Effects plot for temperature- over strain rate-sensitivity ratio. v_0 and ρ_0^α are the main two parameters which affect the temperature over strain rate sensitivity.

6.3.1. *Dislocation network parameters: v_0 and ρ_0^α*

The velocity pre-factor v_0 has a linear relationship with the shear rate, which results in a relatively low influence of this parameter on the yield stress in comparison to the other parameters. This small effect of v_0 may lead to a misinterpretation of its importance. The initial mobile dislocation density ρ_0^α also has a linear relationship with the shear rate. However, due to its dominating influence on the athermal stress component, its effect is generally much higher than v_0 and comparable to the effect of other material parameters. Despite the significant effect of ρ_0^α on the yield stress, a survey of the pertinent literature reveals that its value is often assumed without any critical assessment. In this section, the distinctive role of these two parameters is discussed, and the possibility of finding a unique solution for both is elaborated.

Using Eq. (16) and by assuming τ_μ^α is temperature and strain rate independent, one can determine the relationship for temperature- over strain rate-sensitivity as

$$\frac{\frac{\mathrm{d}\tau^\alpha}{\mathrm{d}T}|_{\dot\gamma^\alpha=const}}{\frac{\mathrm{d}\tau^\alpha}{\mathrm{d}\dot\gamma^\alpha}|_{T=const}} = \frac{|\dot\gamma^\alpha|\log[\frac{|\dot\gamma^\alpha|}{\rho^\alpha b v_0}]}{T}. \tag{23}$$

It can be seen that the temperature- over strain rate-sensitivity ratio itself depends on the temperature and shear rate. This ratio decreases with an increase in temperature for a given shear rate and increases with an increase in the shear rate for a given temperature. However, the only way to alter the temperature- over strain rate-sensitivity ratio for a given temperature and strain rate is an adjustment of $\rho^\alpha b v_0$. In other words, to reach a particular combination of yield stresses at different temperatures and strain rates, this product needs to be adequately determined. Since the Burgers vector is a known parameter, the only open parameters are ρ^α and v_0.

The same conclusion can be derived from the RSM study. Fig. 8 shows the effects plot for temperature- over strain rate-sensitivity ratio at the yield point for two typical cases. Clearly, the most pronounced two parameters which affect the temperature- over strain rate-sensitivity ratio are v_0 and ρ_0^α. Other parameters influence the temperature- over strain rate-sensitivity ratio only through interaction with these two parameters.

These results reveal that it is possible to reach a unique solution for the product $\rho^\alpha v_0$ if the boundary conditions for the optimization are appropriately selected in a way that captures the temperature over strain rate sensitivity. On the other hand, ρ_0^α contributes also to the athermal component of the stress. Therefore, its effects can be distinguished from the effects of v_0. It can be concluded that the value for both parameters can be uniquely determined.

To test this hypothesis, we have performed 50 independent optimization runs. Fig. 9 shows the results for the optimized solutions.

Table 7
Four exemplar optimized solutions with almost similar fitness values. Examples 3 and 4 show the possibility of finding multiple suitable solutions even if one parameter is set to a constant value.

Parameter set	ΔF (J)	τ_0^* (MPa)	p	q	Fitness value
1	1.82×10^{-19}	548	0.30	1.82	11.5
2	1.88×10^{-19}	448	0.27	1.58	11.5
3	1.90×10^{-19}	334	0.25	1.30	11.5
4	2.00×10^{-19}	440	0.25	1.50	11.8

It can be seen that there is a clear convergence for ρ_0^α, and the optimization methodology is able to determine this parameter uniquely. The distribution for ρ_0^α is around 0.2 % of the considered range. The optimization outputs for v_0 are also located in a relatively narrow distribution, i.e. around 5 % of the optimization range. The main reason for the broader range of solutions for v_0 is its small main effect, which results in a negligible error in the stress–strain curves for a change in its value.

It should be noted that the discussion in this section does not mean that the other parameters have no effect on the temperature or strain rate sensitivity of the yield stress. In fact, the barrier parameters mainly determine the temperature and the strain rate sensitivity, while ρ_0^α and v_0 adjust the temperature- over strain rate-sensitivity ratio.

6.3.2. *Barrier parameters: p, q, τ, and ΔF*

Fig. 9 shows the optimized solution for the barrier parameters from 50 independent optimization runs. The barrier parameters define the activation energy for dislocation glide, i.e. $\Delta G = \Delta F(1-(\tau^\alpha/\tau_0^*)^p)^q$. The optimized solutions for τ_0^* and q are distributed in a very wide range, i.e. these parameters do not converge to a unique solution. Besides, p converges to the lower bound of the allowed range. Therefore, also p cannot be considered as a converged parameter despite its narrow distribution. Additional investigations show that, regardless of the selected bounds, p always converges to the lower bound. These additional investigations also show that the value for ΔF depends strongly on the value of p. Hence, also ΔF cannot be considered as a converged parameter despite its narrow distribution. Table 7 shows the values for four exemplar optimized solutions with almost the same fitness value. It is obvious that multiple solutions result in a similar constitutive behavior. It is even possible to find multiple suitable solutions for any other three parameters even when one of the parameters is set to a fixed value. For example, parameter sets 3 and 4 in Table 7 are obtained for a fixed value of $p = 0.25$.

Fig. 10 shows the thermal stress versus temperature for two different sets of parameters. The predicted thermal stresses almost overlap for a wide range of temperatures, and the observed difference is much smaller than the expected experimental errors. Although there is a clear disagreement between the two curves at low temperatures, it is impossible to make a differentiation between these two cases during the optimization procedure due to the lack of experimental data for these temperatures. It can be concluded that no unique solution for the barrier parameters can be achieved using the current set of experimental data.

Even though the difference between the value of the predicted thermal stress is negligible at elevated temperatures, there is a significant difference between the predicted critical temperatures for the two cases given in Fig. 10. As discussed earlier in Section 6.1, ΔF is the only barrier parameter that affects the critical temperature. Therefore, the start of the temperature-insensitive regime is determined solely by ΔF. However, as discussed in Section 6.2, p has a significant effect on thermal stress's flatness when approaching the critical temperature. In other words, for a small p, there is a wide temperature range before the critical temperature where the thermal stress is almost zero. Although p theoretically does not affect the critical temperature, it practically creates a region that is hardly distinguishable from the region above the

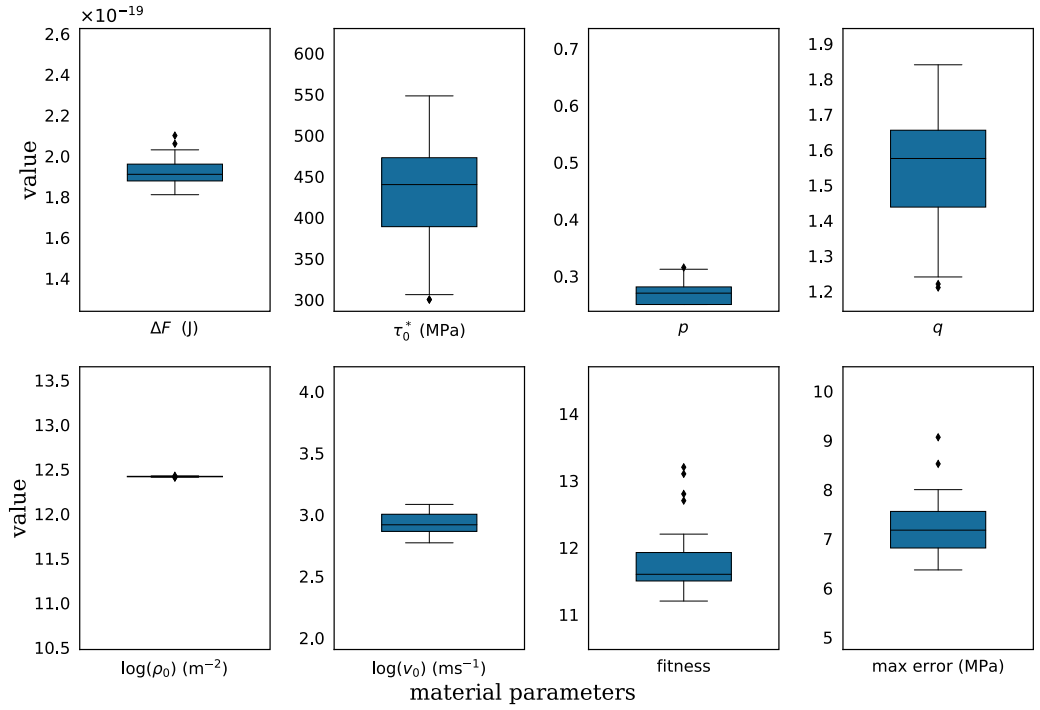

Fig. 9. The optimized solutions from 50 independent optimization runs. The distribution of the fitness value and the maximum observed error in the yield stress prediction shows that the optimized solution from different runs has nearly the same quality. It should be noted that a solution with a lower maximum observed error does not necessarily have a better fitness value, see Eq. (A.9) for how the fitness values are calculated. There is a very good convergence for both ρ_0^a and v_0. However, the optimized solutions for τ_0^* and q are distributed in a very wide range, and these two parameters are not converged to a unique solution. Besides, p converges to the lower bound of the optimization range, and it cannot be considered as a converged parameter despite its narrow distribution. The converged value for ΔF is strongly dependent on the converged value for p. Hence, ΔF also cannot be considered as a converged parameter despite its relatively narrow distribution.

critical temperature. This allows to use a combination of a high ΔF and a small p without any notable change in the thermal stress response. However, both solutions will have a significantly different critical temperatures, see Fig. 10. It can be concluded that an infinite number of numerically equivalent solutions can be found if no assumption about the value of the critical temperature is made.

On the other hand, the decrease of the thermal stress in the low temperature regime depends strongly on q. For different values of τ_0^*, the parameters q and—to some extent—p can be selected in a way to compensate for the difference in the barrier strength for temperatures close to 0 K, see the solid red curve in Fig. 10. Based on this fact and the underdetermined system at high temperatures, different sets of parameters result in a very similar behavior over a vast range of temperatures. Therefore, it is not possible to find a unique set of parameters without any assumption about the values for either τ_0^* or ΔF.

This issue is mainly because p and q are introduced into the equations in a purely phenomenological way to relate ΔG to ΔF. Originally, Eq. (10) has been derived for a barrier with a rectangular profile, i.e. $p = 1.0$ and $q = 1.0$. Therefore, ΔF is related to τ_0^* as $\Delta F = \tau_0^* b l^2$. This results in a linear relationship between thermal stress and temperature, which is physically not plausible. Introduction of p and q allows to add curvature to the thermal stress curve. As a result of how p and q are introduced into the equations, it is no longer possible to physically relate τ_0^* and ΔF. This results in a situation where the critical temperature is completely independent of τ_0^*. Therefore, the system becomes an underdetermined system for a vast range of temperatures, and the only way to uniquely determine all four parameters will be by knowing both the critical temperature and the barrier's strength.

Due to many uncertainties and complexities in the deformation behavior at high temperatures, the critical temperature cannot be determined with certainty. Moreover, experiments at temperatures close to 0 K are needed to determine τ_0^*, which is not an easy and routine experiment to perform. Therefore, neither T_c nor τ_0^* is easy to determine experimentally. Consequently, reaching a unique solution for the barrier parameters is very challenging.

One way to partially overcome this issue is by constraining the critical temperature. Although it is difficult to determine the critical temperature precisely, a range for the critical temperature can be estimated based on the rate of change in the yield stress with temperature. This estimated range can be used along with Eq. (18) to constrain the critical temperature.

As discussed earlier in Section 5.1.1, the inflection point in the yield stress versus deformation temperature curve may correspond to the activation of a new softening mechanism. However, before the inflection point, the rate of change in the yield stress with temperature is decreased considerably, and the experimental data show a tendency to reach a plateau. It can be expected that the critical temperature lies in the vicinity but higher than the inflection point. The inflection points determined in this study are 725, 688, and 656 K for the strain rates of 1.0, 0.1, and 0.01 s^{-1}, respectively. Hence, the critical temperature range is here selected to be between 600 to 900 K. The upper limit is selected high enough to prevent over constraining the critical temperature.

Fig. 11 shows the optimized solutions from 50 independent optimization runs when the critical temperature is constrained. It can be seen that the distribution for p is still relatively narrow, around 10% of the optimization range, and p is no longer converging to the lower bound. Consequently, the values achieved for ΔF also can be considered as adequately converged solutions. The optimization outputs for ΔF are distributed in a range around 5% of the optimization range. The width of the distribution for τ_0^* and q is noticeably smaller than for the unconstrained case. However, these distributions are still too wide to be considered as converged solutions. It can be concluded that constraining the critical temperature is partially solving the problem at high temperatures. It also improves the results for τ_0^* and q. However,

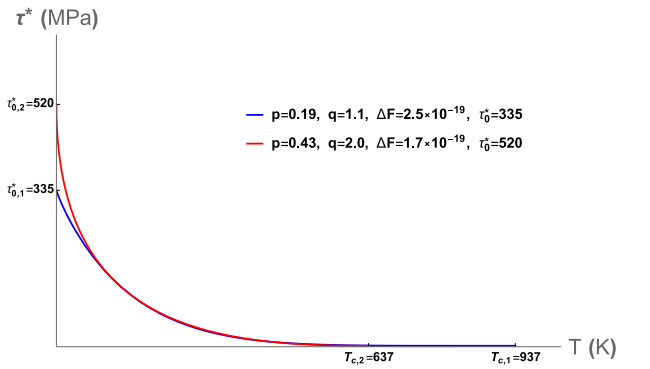

Fig. 10. Thermal stress versus temperature for two different sets of parameters. Although there is a clear disagreement between the two curves at very low temperatures and the estimated critical temperature, the predicted thermal stresses almost overlap for a wide range of temperatures.

it seems that the system is still underdetermined, especially at low temperatures. Therefore, to fully solve the issue, experimental data at much lower temperatures are required. Constraining the critical temperature does not noticeably affect the distribution for ρ_0^α and v_0.

The main reason for introducing p and q in the way outlined in this section is the simplicity of the equations. An alternative approach to fundamentally overcome the non-uniqueness issue is by using a mathematically reasonable profile for the barrier, such as a sinusoidal profile. In this case, ΔG can be estimated directly from the barrier's profile by calculating the activation volume for dislocation glide. This overcomes the need to introduce the curvature in thermal stress by phenomenological parameters like p and q. Although such a barrier profile results in more complex equations for the constitutive law, it reduces the number of *phenomenological* material parameters by one or two. This can be a significant advantage for physics-based models, which generally have a large number of material parameters. Evaluating such an approach is, however, beyond the scope of this manuscript.

7. Conclusions

In this study, the material parameters for a physics-based crystal plasticity model were identified using macroscopic stress–strain curve data experimentally obtained for IF steel. The uniqueness of the parameters was studied, and an in-depth analysis of the parameters was provided. Since the temperature-dependent motion of dislocations of the constitutive law used in this study has the same basis as the one proposed by Kocks et al. (1975), most of the conclusions made in this study are expandable to many other models that use the same concept.

The following conclusions can be drawn:

- The dislocation-density-based constitutive law is capable of predicting the polycrystal yield stress behavior over a wide range of temperatures and strain rates with a single set of material parameters. However, it fails to predict the material response at very high temperatures correctly.
- The temperature-dependent crystal plasticity model is not numerically stable at temperatures close to or above the critical temperature if only the waiting time is considered in the formulation of the dislocation velocity. The formulation can be modified and stabilized at high temperatures by adding the running time into the formulations.
- The ranges provided for p and q, parameters which determine the shape of the short-range barrier, in the literature are rather wide and include unphysical barrier profiles. New limits for these two parameters are provided.
- Initial dislocation density ρ_0^α and dislocation glide velocity prefactor v_0 are determining the temperature- over strain rate-sensitivity ratio. Due to this distinct role of the two parameters, it is possible to determine them uniquely.
- The barrier parameters are the main variables in determining the stress response at the yield point. The temperature and strain rate sensitivity is also mainly controlled by them.
- The system is underdetermined for the barrier parameters. Prior knowledge about the barrier's strength and the critical temperature is necessary to uniquely determine these parameters.

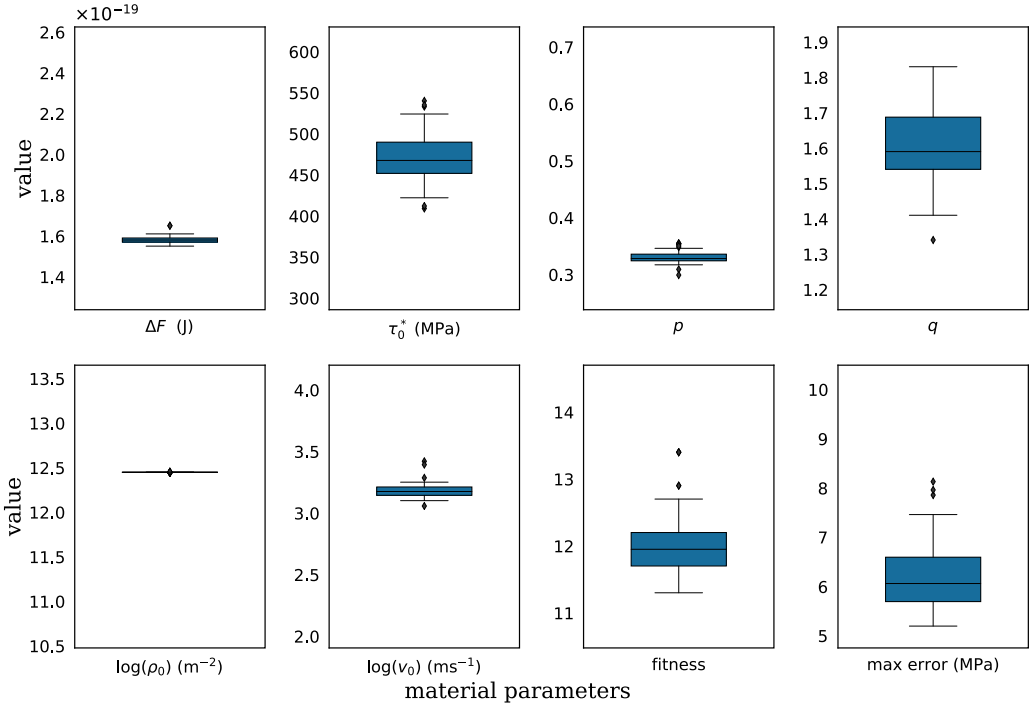

Fig. 11. The optimized solutions from 50 independent optimization runs for constrained critical temperature. Constraining the critical temperature is partially solving the issue of having an underdetermined system at high temperatures. Besides, it improves the results for τ_0^* and q. However, the system is still underdetermined, especially at low temperatures.

- Although the critical temperature is theoretically independent of the shape of the barrier, it is practically altered by the material parameter p.

CRediT authorship contribution statement

Karo Sedighiani: Conceptualization, Methodology, Software, Validation, Formal analysis, Investigation, Writing – original draft, Visualization. **Konstantina Traka:** Visualization, Validation, Writing – original draft. **Franz Roters:** Software, Resources, Data curation, Writing – review & editing, Supervision. **Dierk Raabe:** Resources, Writing – review & editing, Supervision, Project administration, Funding acquisition. **Jilt Sietsma:** Resources, Writing – review & editing, Supervision, Project administration, Funding acquisition. **Martin Diehl:** Methodology, Formal analysis, Software, Data curation, Writing – original draft, Visualization, Supervision.

Declaration of competing interest

The authors declare that they have no known competing financial interests or personal relationships that could have appeared to influence the work reported in this paper.

Data availability

The experimental data required to reproduce these findings are available to download from ExperimentalData. The optimization methodology has been implemented into DAMASK (damask.mpie.de) and is available as free and open source software at git.damask.mpie.de.

Acknowledgments

This research was carried out under project number S41.5.15572a in the framework of the Partnership Program of the Materials innovation institute M2i (www.m2i.nl) and the Technology Foundation TTW (www.stw.nl), which is part of the Netherlands Organization for Scientific Research (www.nwo.nl). The authors are grateful to Kees Bos (Tata Steel) for providing the materials for the experiments. F.R. and M.D. acknowledge the discussion with the participants of the workshop *Mechanics of Materials: Towards Predictive Methods for Kinetics in Plasticity, Fracture, and Damage* at the Mathematisches Forschungsinstitut Oberwolfach (MFO, Oberwolfach Research Institute for Mathematics) (Roters et al., 2020).

Appendix A. Parameter identification methodology

A.1. Genetic algorithm

Genetic algorithms (GA) are randomized search optimization methods based on the principles of natural selection and evolution processes (Goldberg, 1989; Beg and Islam, 2016). In a GA, the first step is to randomly select a number of chromosomes to create an initial population. A chromosome, $\boldsymbol{\Theta}$, is a potential solution for the optimization problem, and it is made up of a number of genes, Θ_i,

$$\boldsymbol{\Theta} = (\Theta_1, \Theta_2, \dots, \Theta_k),$$

A *gene* is an adjustable parameter that is needed to be identified, i.e. here a material parameter.

In the next steps of a GA, the chromosomes are manipulated to produce new generations. These steps involve the selection and evaluation of chromosomes inspired by natural processes like crossover and mutation. In the previous work by the authors, (Sedighiani et al., 2020), the details of the processes used in this study are outlined.

A.1.1. Genetic algorithm processes

Selection

A chromosome with a better fitness value has a higher chance of being a parent, which mates and recombines to create offspring for the next generation. In this study, the rank-based wheel approach is used for selecting pairs of parents. According to this approach, the selection is solely based on the relative ranking of the chromosomes in the population.

Crossover

Crossover is an operation in which a pair of chromosomes swap their genes to generate a new pair of offspring. For this study, the reduced surrogate methods is used. In this approach, the chromosomes of both parents are divided into two parts. The division is applied at the same position for both parents which is selected randomly under the condition that each part contains at least one gene. The genes up to the division point for each parent are then combined with the remaining genes of the other parent to generate a pair of offspring. However, the division is limited to those positions which result in offsprings with different genes.

Mutation

Mutation randomly changes one or more genes in a chromosome with a probability equal to the mutation rate. Mutation is used to maintain diversity during evolution of the population. Diversity helps to avoid local minima by preventing the generations from becoming very similar.

Elitist selection

By means of elitist selection a small proportion of the best chromosomes from the current generation is preserved and passed without any changes to the next generation. Elitist selection increases the performance as it ensures that the achievement is not lost from one generation to the next. The elite chromosomes are not allowed to be crossed over or subjected to mutation. However, the elite chromosomes are eligible for selection as parents.

A.2. Approximate evaluation function: response surface methodology

In a GA, the objective functions need to be evaluated repeatedly to determine the quality of chromosomes, i.e. the potential solutions. This makes GAs time-consuming for computationally expensive evaluation functions, here, the CP simulations. To overcome this problem, Sedighiani et al. (2020) evaluated the fitness of the chromosomes using a cost-effective approximate evaluation function based on the response surface methodology (RSM).

The RSM is a statistical method that gives the relationship between explanatory variables and response variables (Moran et al., 2004; Bezerra et al., 2008). In this paper, the adjustable constitutive parameters are the explanatory variables, and the stress is the response variable. The deformation temperature, the strain rate, and the applied strain are independent (conditional) input variables. RSM is especially helpful when an explanatory variable's effects depend on the levels of the other explanatory variables.

In RSM, a function (typically a polynomial) fitted to a set of support points is used to approximate the response variable as a function of the explanatory variables. In this paper, a second-order polynomial, including up to four-way interaction effects, is used:

$$\begin{aligned}\hat{\sigma} = \beta_0 &+ \sum_{i=1}^{k} \beta_i \theta_i + \sum_{i=1}^{k} \beta_{ii} \theta_i^2 + \sum_{1 \le i < j}^{k} \beta_{ij} \theta_i \theta_j + \sum_{1 \le i < j < l}^{k} \beta_{ijl} \theta_i \theta_j \theta_l \\ &+ \sum_{1 \le i < j < l < m}^{k} \beta_{ijlm} \theta_i \theta_j \theta_l \theta_m + e \qquad i \neq j \neq l,\end{aligned}$$

where $\hat{\sigma}$ is the response variable, and θ_i is the normalized value for explanatory variable (i.e. gene) Θ_i:

$$\theta_i = \frac{\Theta_i - \Theta_i^m}{\Theta_i^s}, \tag{A.1}$$

where Θ_i^s and Θ_i^m are respectively the span and center point of the range for Θ_i.

The last term in Eq. (A.1) (e) represents the error, i.e. the difference between the predicted values and the observed results. β_0 is the constant effect. β_i is the main effect of parameter θ_i which determines the significance of the variable. β_{ij}, β_{ijl}, and β_{ijlm} are two-way, three-way, and four-way interaction effects, respectively. β_{ii} are curvilinear effects.

Eq. (A.1) can be rewritten in matrix notation as:

$$\mathbf{Y}_{\hat{\sigma}} = \mathbf{X}_\theta \boldsymbol{\beta} + \mathbf{E}, \tag{A.2}$$

where $\mathbf{Y}_{\hat{\sigma}}$ is the response matrix, $\mathbf{X}_\theta$ is the full experimental design matrix, $\boldsymbol{\beta}$ is the full parameter matrix, and $\mathbf{E}$ is the error matrix. The matrix $\boldsymbol{\beta}$ can be calculated using the least squares method (Bezerra et al., 2008) to minimize the residual:

$$\boldsymbol{\beta} = (\mathbf{X}_\theta^T \mathbf{X}_\theta)^{-1} (\mathbf{X}_\theta^T \mathbf{Y}_{\hat{\sigma}}). \tag{A.3}$$

The RSM requires a series of designed simulations to approximate the response. Here, the face-centered composite design is employed to build this off-line database, which allows us to build up a second-order polynomial model (Moran et al., 2004; Bezerra et al., 2008). For more detail on this methodology, see Sedighiani et al. (2020).

A.3. Objective functions and fitness

A fitness value is determined for each chromosome in the population, which signifies the chromosomes' capability in reproducing the target response, here, the stress–strain curves measured experimentally. For this purpose, four types of objective functions are used to estimate the difference between the result obtained using a specific chromosome and the target function.

Objective functions

The first objective function measures the difference between the simulated stress at selected strain values and the experimentally determined stress:

$$d_1^m(\boldsymbol{\Theta}, T, \dot{\varepsilon}) = \sqrt{\frac{\sum_{i=0}^{N} (\hat{\sigma}_i(\boldsymbol{\Theta}, T, \dot{\varepsilon}) - \sigma_i(T, \dot{\varepsilon}))^2}{\sum_{i=0}^{N} \sigma_i(T, \dot{\varepsilon})^2}}, \tag{A.4}$$

where σ_i is the stress experimentally measured at strain level ε_i, and N is the total number of all strain levels considered. $\hat{\sigma}_i$ is the stress response predicted for the potential solution $\boldsymbol{\Theta}$.

The second type of objective function measures the difference between the average slope of the response and the experimentally observed stress–strain curves:

$$d_2^m(\boldsymbol{\Theta}, T, \dot{\varepsilon}) = \left| \frac{\left(\hat{\sigma}_N(\boldsymbol{\Theta}, T, \dot{\varepsilon}) - \hat{\sigma}_0(\boldsymbol{\Theta}, T, \dot{\varepsilon})\right) - \left(\sigma_N(T, \dot{\varepsilon}) - \sigma_0(T, \dot{\varepsilon})\right)}{\sigma_N(T, \dot{\varepsilon}) - \sigma_0(T, \dot{\varepsilon})} \right|, \tag{A.5}$$

where indices 0 and N represent the yield strain and the maximum evaluated strain, respectively. This objective function returns zero error for two parallel stress–strain curves.

In addition to the above mentioned objective functions, two additional objective functions are defined, an objective function to measure the strain rate sensitivity:

$$d_3^m(\boldsymbol{\Theta}, T, \dot{\varepsilon}_k, \dot{\varepsilon}_l) = \sqrt{\frac{\sum_{i=0}^{N} \left[(\hat{\sigma}_i(\boldsymbol{\Theta}, T, \dot{\varepsilon}_l) - \hat{\sigma}_i(\boldsymbol{\Theta}, T, \dot{\varepsilon}_k)) - (\sigma_i(T, \dot{\varepsilon}_l) - \sigma_i(T, \dot{\varepsilon}_k))\right]^2}{\sum_{i=0}^{N} (\sigma_i(T, \dot{\varepsilon}_l) - \sigma_i(T, \dot{\varepsilon}_k))^2}}, \tag{A.6}$$

and an objective function to measure the temperature sensitivity:

$$d_4^m(\boldsymbol{\Theta}, T_l, T_k, \dot{\varepsilon}) = \sqrt{\frac{\sum_{i=0}^{N} [(\hat{\sigma}_i(\boldsymbol{\Theta}, T_k, \dot{\varepsilon}) - \hat{\sigma}_i(\boldsymbol{\Theta}, T_l, \dot{\varepsilon})) - (\sigma_i(T_k, \dot{\varepsilon}) - \sigma_i(T_l, \dot{\varepsilon}))]^2}{\sum_{i=0}^{N} (\sigma_i(T_k, \dot{\varepsilon}) - \sigma_i(T_l, \dot{\varepsilon}))^2}}, \tag{A.7}$$

where (T_l, T_k) and $(\dot{\varepsilon}_k, \dot{\varepsilon}_l)$ represent different combinations of temperatures and strain rates, respectively.

Fitness

The distance between the experimental and simulated data estimated using the objective functions defined in Eq. (A.4) to Eq. (A.7) is only for one loading condition. For each types of objective function mentioned above, the total normalized distance under all M considered loading conditions is calculated as:

$$D_j(\boldsymbol{\Theta}) = \sum_{m=1}^{M} d_j^m(\boldsymbol{\Theta}, T, \dot{\varepsilon}), \qquad j = 1, 2, 3, 4, \tag{A.8}$$

Eventually, the four types of objective functions are combined to obtain a unified fitness value for a chromosome:

$$F(\boldsymbol{\Theta}) = \sum_{j=1}^{4} w_j \, D_j(\boldsymbol{\Theta}), \tag{A.9}$$

where w_j are weights for each type of objective functions.

References

Adams, J.J., Agosta, D.S., Leisure, R.G., Ledbetter, H., 2006. Elastic constants of monocrystal iron from 3 to 500 K. J. Appl. Phys. (ISSN: 00218979) 100 (11), http://dx.doi.org/10.1063/1.2365714.

Addessio, F.L., Luscher, D.J., Cawkwell, M.J., Ramos, K.J., 2017. A single-crystal model for the high-strain rate deformation of cyclotrimethylene trinitramine including phase transformations and plastic slip. J. Appl. Phys. (ISSN: 10897550) 121 (18), http://dx.doi.org/10.1063/1.4983009.

Alankar, A., Field, D.P., Raabe, D., 2014. Plastic anisotropy of electro-deposited pure α-iron with sharp crystallographic <1 1 1>// texture in normal direction: Analysis by an explicitly dislocation-based crystal plasticity model. Int. J. Plast. (ISSN: 07496419) 52, 18–32. http://dx.doi.org/10.1016/j.ijplas.2013.03.006.

Alankar, A., Mastorakos, I.N., Field, D.P., 2009. A dislocation-density-based 3D crystal plasticity model for pure aluminum. Acta Mater. (ISSN: 13596454) 57 (19), 5936–5946. http://dx.doi.org/10.1016/j.actamat.2009.08.028.

Amirkhizi, A.V., Nemat-Nasser, S., 2007. A framework for numerical integration of crystal elasto-plastic constitutive equations compatible with explicit finite element codes. Int. J. Plast. (ISSN: 07496419) 23 (10–11), 1918–1937. http://dx.doi.org/10.1016/j.ijplas.2007.05.003.

Arsenlis, A., Parks, D.M., 2002. Modeling the evolution of crystallographic dislocation density in crystal plasticity. J. Mech. Phys. Solids (ISSN: 00225096) 50 (9), 1979–2009. http://dx.doi.org/10.1016/S0022-5096(01)00134-X.

Aubry, S., Fitzgerald, S.P., Dudarev, S.L., Cai, W., 2011. Equilibrium shape of dislocation shear loops in anisotropic α-Fe. Modelling Simulation Mater. Sci. Eng. (ISSN: 09650393) 19 (6), http://dx.doi.org/10.1088/0965-0393/19/6/065006.

Becker, R., 1991. Analysis of texture evolution in channel die compression—I. Effects of grain interaction. Acta Metallurgica Et Materialia (ISSN: 09567151) 39 (6), 1211–1230. http://dx.doi.org/10.1016/0956-7151(91)90209-J.

Beg, A.H., Islam, M.Z., 2016. Advantages and limitations of genetic algorithms for clustering records. In: Proceedings of the 2016 IEEE 11th Conference on Industrial Electronics and Applications. ICIEA 2016, pp. 2478–2483. http://dx.doi.org/10.1109/ICIEA.2016.7604009.

Bertin, M., Du, C., Hoefnagels, J.P.M., Hild, F., 2016. Crystal plasticity parameter identification with 3D measurements and integrated digital image correlation. Acta Mater. (ISSN: 13596454) 116, 321–331. http://dx.doi.org/10.1016/j.actamat.2016.06.039.

Bezerra, M.A., Santelli, R.E., Oliveira, E.P., Villar, Le.S., Escaleira, L.A., 2008. Response surface methodology (RSM) as a tool for optimization in analytical chemistry. Talanta (ISSN: 00399140) 76 (5), 965–977. http://dx.doi.org/10.1016/j.talanta.2008.05.019.

Blum, W., Eisenlohr, P., 2009. Dislocation mechanics of creep. Mater. Sci. Eng. A (ISSN: 09215093) 510–511 (C), 7–13. http://dx.doi.org/10.1016/j.msea.2008.04.110.

Castelluccio, G.M., Geller, C.B., McDowell, D.L., 2018. A rationale for modeling hydrogen effects on plastic deformation across scales in FCC metals. Int. J. Plast. (ISSN: 07496419) 111, http://dx.doi.org/10.1016/j.ijplas.2018.07.009.

Castelluccio, G.M., McDowell, D.L., 2017. Mesoscale cyclic crystal plasticity with dislocation substructures. Int. J. Plast. (ISSN: 07496419) 98, http://dx.doi.org/10.1016/j.ijplas.2017.06.002.

Cereceda, D., Diehl, M., Roters, F., Raabe, D., Perlado, J.M., Marian, J., 2016. Unraveling the temperature dependence of the yield strength in single-crystal tungsten using atomistically-informed crystal plasticity calculations. Int. J. Plast. (ISSN: 07496419) 78, 242–265. http://dx.doi.org/10.1016/j.ijplas.2015.09.002.

Chakraborty, P., Bulent Biner, S., 2016. Crystal plasticity modeling of irradiation effects on flow stress in pure-iron and iron-copper alloys. Mech. Mater. (ISSN: 01676636) 101, http://dx.doi.org/10.1016/j.mechmat.2016.07.013.

Cheong, K., Busso, E.P., 2004. Discrete dislocation density modelling of single phase FCC polycrystal aggregates. Acta Mater. (ISSN: 13596454) 52 (19), 5665–5675. http://dx.doi.org/10.1016/j.actamat.2004.08.044.

Dever, D.J., 1972. Temperature dependence of the elastic constants in α-iron single crystals: Relationship to spin order and diffusion anomalies. J. Appl. Phys. (ISSN: 00218979) 43 (8), 3293–3301. http://dx.doi.org/10.1063/1.1661710.

Diehl, M., Wang, D., Liu, C., Rezaei Mianroodi, J., Han, F., Ma, D., Kok, P.J.J., Roters, F., Shanthraj, P., 2020. Solving material mechanics and multiphysics problems of metals with complex microstructures using DAMASK—The Düsseldorf advanced material simulation kit. In: Advanced Engineering Materials, Vol. 22. (3), (ISSN: 15272648).

Doncaster, C.P., Davey, A.J.H., 2007. Analysis of Variance and Covariance: How to Choose and Construct Models for the Life Sciences. http://dx.doi.org/10.1017/CBO9780511611377.

Eisenlohr, P., Diehl, M., Lebensohn, R.A., Roters, F., 2013. A spectral method solution to crystal elasto-viscoplasticity at finite strains. Int. J. Plast. (ISSN: 07496419) 46, 37–53. http://dx.doi.org/10.1016/j.ijplas.2012.09.012.

Eisenlohr, P., Roters, F., 2008. Selecting a set of discrete orientations for accurate texture reconstruction. Comput. Mater. Sci. (ISSN: 09270256) 42 (4), 670–678. http://dx.doi.org/10.1016/j.commatsci.2007.09.015.

Evers, L.P., Brekelmans, W.A.M., Geers, M.G.D., 2004a. Non-local crystal plasticity model with intrinsic SSD and gnd effects. J. Mech. Phys. Solids (ISSN: 00225096) 52 (10), 2379–2401. http://dx.doi.org/10.1016/j.jmps.2004.03.007.

Evers, L.P., Brekelmans, W.A.M., Geers, M.G.D., 2004b. Scale dependent crystal plasticity framework with dislocation density and grain boundary effects. Int. J. Solids Struct. (ISSN: 00207683) 41 (18–19), 5209–5230. http://dx.doi.org/10.1016/j.ijsolstr.2004.04.021.

Evers, L.P., Parks, D.M., Brekelmans, W.A.M., Geers, M.G.D., 2002. Crystal plasticity model with enhanced hardening by geometrically necessary dislocation accumulation. J. Mech. Phys. Solids (ISSN: 00225096) 50 (11), 2403–2424. http://dx.doi.org/10.1016/S0022-5096(02)00032-7.

Fitzgerald, S.P., 2010. Frank-read sources and the yield of anisotropic cubic crystals. Phil. Mag. Lett. (ISSN: 09500839) 90 (3), http://dx.doi.org/10.1080/09500830903571392.

Fitzgerald, S.P., Dudarev, S.L., 2008. Dislocation pile-ups in Fe at high temperature. Proc. R. Soc. A: Math. Phys. Eng. Sci. (ISSN: 14712946) 464 (2098), http://dx.doi.org/10.1098/rspa.2008.0116.

Ghosh, S., Weber, G., Keshavarz, S., 2016. Multiscale modeling of polycrystalline nickel-based superalloys accounting for subgrain microstructures. Mech. Res. Commun. (ISSN: 00936413) 78, http://dx.doi.org/10.1016/j.mechrescom.2015.12.001.

Goldberg, D.E., 1989. Genetic Algorithms in Search, Optimization and Machine Learning, first ed. Addison-Wesley Longman Publishing Co., Inc..

Ha, S., Jang, J.H., Kim, K.T., 2017. Finite element implementation of dislocation-density-based crystal plasticity model and its application to pure aluminum crystalline materials. Int. J. Mech. Sci. (ISSN: 00207403) 120 (October 2016), 249–262. http://dx.doi.org/10.1016/j.ijmecsci.2016.11.011.

Hansen, B.L., Beyerlein, I.J., Bronkhorst, C.A., Cerreta, E.K., Dennis-Koller, D., 2013. A dislocation-based multi-rate single crystal plasticity model. Int. J. Plast. (ISSN: 07496419) 44, http://dx.doi.org/10.1016/j.ijplas.2012.12.006.

Hill, R., 1952. The elastic behaviour of a crystalline aggregate. Proc. Phys. Soc. Sect. A (ISSN: 03701298) 65 (5), http://dx.doi.org/10.1088/0370-1298/65/5/307.

Hutchinson, J.W., 1976. Bounds and self-consistent estimates for creep of polycrystalline materials. Proceedings of the Royal Society A: Mathematical, Physical and Engineering Sciences (ISSN: 1364-5021) 348 (1652), 101–127. http://dx.doi.org/10.1098/rspa.1976.0027.

Keshavarz, S., Ghosh, S., 2013. Multi-scale crystal plasticity finite element model approach to modeling nickel-based superalloys. Acta Mater. (ISSN: 13596454) 61 (17), http://dx.doi.org/10.1016/j.actamat.2013.07.038.

Keshavarz, S., Ghosh, S., 2015. Hierarchical crystal plasticity FE model for nickel-based superalloys: Sub-grain microstructures to polycrystalline aggregates. Int. J. Solids Struct. (ISSN: 00207683) 55, http://dx.doi.org/10.1016/j.ijsolstr.2014.03.037.

Keshavarz, S., Ghosh, S., Reid, A.C.E., Langer, S.A., 2016. A non-schmid crystal plasticity finite element approach to multi-scale modeling of nickel-based superalloys. Acta Mater. (ISSN: 13596454) 114, 106–115. http://dx.doi.org/10.1016/j.actamat.2016.05.016.

Khan, A.S., Liu, J., Yoon, J.W., Nambori, R., 2015. Strain rate effect of high purity aluminum single crystals: Experiments and simulations. Int. J. Plast. (ISSN: 07496419) 67, 39–52. http://dx.doi.org/10.1016/j.ijplas.2014.10.002.

Kocks, U.F., Argon, A.S., Ashby, M.F., 1975. Thermodynamics and Kinetics of Slip. Pergamon Press.

Li, D., Zbib, H., Sun, X., Khaleel, M., 2014. Predicting plastic flow and irradiation hardening of iron single crystal with mechanism-based continuum dislocation dynamics. Int. J. Plast. (ISSN: 07496419) 52, http://dx.doi.org/10.1016/j.ijplas.2013.01.015.

Luscher, D.J., Addessio, F.L., Cawkwell, M.J., Ramos, K.J., 2017. A dislocation density-based continuum model of the anisotropic shock response of single crystal α-cyclotrimethylene trinitramine. J. Mech. Phys. Solids (ISSN: 00225096) 98, http://dx.doi.org/10.1016/j.jmps.2016.09.005.

Ma, A., Roters, F., 2004. A constitutive model for fcc single crystals based on dislocation densities and its application to uniaxial compression of aluminium single crystals. Acta Mater. (ISSN: 13596454) 52 (12), 3603–3612. http://dx.doi.org/10.1016/j.actamat.2004.04.012.

Ma, A., Roters, F., Raabe, D., 2006a. A dislocation density based constitutive model for crystal plasticity FEM including geometrically necessary dislocations. Acta Mater. (ISSN: 13596454) 54 (8), 2169–2179. http://dx.doi.org/10.1016/j.actamat.2006.01.005.

Ma, A., Roters, F., Raabe, D., 2006b. On the consideration of interactions between dislocations and grain boundaries in crystal plasticity finite element modeling – theory, experiments, and simulations. Acta Mater. (ISSN: 13596454) 54 (8), 2181–2194. http://dx.doi.org/10.1016/j.actamat.2006.01.004.

Madec, R., Kubin, L.P., 2017. Dislocation strengthening in FCC metals and in BCC metals at high temperatures. Acta Mater. (ISSN: 13596454) 126, 166–173. http://dx.doi.org/10.1016/j.actamat.2016.12.040.

Mandal, S., T. Gockel, B., Rollett, A.D., 2017. Application of canonical correlation analysis to a sensitivity study of constitutive model parameter fitting. Mater. Des. (ISSN: 18734197) 132, 30–43. http://dx.doi.org/10.1016/j.matdes.2017.06.050.

Monnet, G., Vincent, L., Devincre, B., 2013. Dislocation-dynamics based crystal plasticity law for the low- and high-temperature deformation regimes of bcc crystal. Acta Mater. (ISSN: 13596454) 61 (16), 6178–6190. http://dx.doi.org/10.1016/j.actamat.2013.07.002.

Moran, L., Hanlon, L., Von Kienlin, A., McBreen, B., McBreen, S., McGlynn, S., French, J., Preece, R., Kaneko, Y., Williams, O.R., Bennett, K., Kippen, R.M., 2004. Preliminary integral analysis of GRB 040106. (552), European Space Agency, (Special Publication) ESA SP, (ISSN: 03796566) pp. 653–656. http://dx.doi.org/10.1088/1751-8113/44/8/085201.

Nemat-Nasser, S., Okinaka, T., Ni, L., 1998. A physically-based constitutive model for BCC crystals with application to polycrystalline tantalum. J. Mech. Phys. Solids (ISSN: 00225096) 46 (6), 1009–1038. http://dx.doi.org/10.1016/S0022-5096(97)00064-1.

Ono, K., 1968. Temperature dependence of dispersed barrier hardening. J. Appl. Phys. (ISSN: 00218979) 39 (3), http://dx.doi.org/10.1063/1.1656434.

Orowan, E., 1934. Zur Kristallplastizität. III - Über den mechanismus des gleitvorganges. Z. Phys. (ISSN: 14346001) 89 (9–10), 634–659. http://dx.doi.org/10.1007/BF01341480.

Patra, A., McDowell, D.L., 2012. Crystal plasticity-based constitutive modelling of irradiated bcc structures. Phil. Mag. (ISSN: 1478-6435) 92 (7), 861–887. http://dx.doi.org/10.1080/14786435.2011.634855.

Patra, A., McDowell, D.L., 2013. Continuum modeling of localized deformation in irradiated bcc materials. J. Nucl. Mater. (ISSN: 00223115) 432 (1–3), 414–427. http://dx.doi.org/10.1016/j.jnucmat.2012.08.021.

Patra, A., McDowell, D.L., 2016. Crystal plasticity investigation of the microstructural factors influencing dislocation channeling in a model irradiated bcc material. Acta Mater. (ISSN: 13596454) 110, 364–376. http://dx.doi.org/10.1016/j.actamat.2016.03.041.

Patra, A., Zhu, T., McDowell, D.L., 2014. Constitutive equations for modeling non-schmid effects in single crystal bcc-Fe at low and ambient temperatures. Int. J. Plast. (ISSN: 07496419) 59, 1–14. http://dx.doi.org/10.1016/j.ijplas.2014.03.016.

Peirce, D., Asaro, R.J., Needleman, A., 1982. An analysis of nonuniform and localized deformation in ductile single crystals. Acta Metall. (ISSN: 00016160) 30 (6), 1087–1119. http://dx.doi.org/10.1016/0001-6160(82)90005-0.

Pokharel, R., Patra, A., Brown, D.W., Clausen, B., Vogel, S.C., Gray, G.T., 2019. An analysis of phase stresses in additively manufactured 304l stainless steel using neutron diffraction measurements and crystal plasticity finite element simulations. Int. J. Plast. (ISSN: 07496419) 121, 201–217. http://dx.doi.org/10.1016/j.ijplas.2019.06.005.

Raabe, D., Sachtleber, M., Zhao, Z., Roters, F., Zaefferer, S., 2001. Micromechanical and macromechanical effects in grain scale polycrystal plasticity experimentation and simulation. Acta Mater. (ISSN: 13596454) 49 (17), 3433–3441. http://dx.doi.org/10.1016/S1359-6454(01)00242-7.

Regazzoni, G., Kocks, U.F., Follansbee, P.S., 1987. Dislocation kinetics at high strain rates. Acta Metall. (ISSN: 00016160) 35 (12), 2865–2875. http://dx.doi.org/10.1016/0001-6160(87)90285-9.

Reuber, C., Eisenlohr, P., Roters, F., Raabe, D., 2014. Dislocation density distribution around an indent in single-crystalline nickel: Comparing nonlocal crystal plasticity finite-element predictions with experiments. Acta Mater. (ISSN: 13596454) 71, 333–348. http://dx.doi.org/10.1016/j.actamat.2014.03.012.

Reuss, A., 1929. Berechnung der Fließgrenze von Mischkristallen auf Grund der Plastizitätsbedingung für einkristalle. Z. Angew. Math. Mech. (ISSN: 15214001) 9 (1), 49–58. http://dx.doi.org/10.1002/zamm.19290090104.

Roters, F., Diehl, M., Sedighiani, K., 2020. (Re-) formulation of dislocation density based crystal plasticity models in view of insights from parameter determination. In: Kienzler, R., McDowell, D.L., Müller, S., Werner, E. (Eds.), Oberwolfach Reports, Vol. 17. European Mathematical Society Publishing House, Zürich, http://dx.doi.org/10.14760/OWR-2020-13.

Roters, F., Diehl, M., Shanthraj, P., Eisenlohr, P., Reuber, C., Wong, S.L., Maiti, T., Ebrahimi, A., Hochrainer, T., Fabritius, H.O., Nikolov, S., Friák, M., Fujita, N., Grilli, N., Janssens, K.G.F., Jia, N., Kok, P.J.J., Ma, D., Meier, F., Werner, E., Stricker, M., Weygand, D., Raabe, D., 2019. DAMASK – The Düsseldorf advanced material simulation kit for modeling multi-physics crystal plasticity, thermal, and damage phenomena from the single crystal up to the component scale. Comput. Mater. Sci. (ISSN: 09270256) 158, 420–478. http://dx.doi.org/10.1016/j.commatsci.2018.04.030.

Roters, F., Eisenlohr, P., Hantcherli, L., Tjahjanto, D.D., Bieler, T.R., Raabe, D., 2010. Overview of constitutive laws, kinematics, homogenization and multiscale methods in crystal plasticity finite-element modeling: Theory, experiments, applications. Acta Mater. (ISSN: 13596454) 58 (4), 1152–1211. http://dx.doi.org/10.1016/j.actamat.2009.10.058.

Sedighiani, K., Diehl, M., Traka, K., Roters, F., Sietsma, J., Raabe, D., 2020. An efficient and robust approach to determine material parameters of crystal plasticity constitutive laws from macro-scale stress–strain curves. Int. J. Plast. (ISSN: 07496419) 134, 102779. http://dx.doi.org/10.1016/j.ijplas.2020.102779.

Shanthraj, P., Diehl, M., Eisenlohr, P., Roters, F., Raabe, D., 2019. Spectral solvers for crystal plasticity and multi-physics simulations. In: Handbook of Mechanics of Materials. http://dx.doi.org/10.1007/978-981-10-6884-3_80.

Shanthraj, P., Eisenlohr, P., Diehl, M., Roters, F., 2015. Numerically robust spectral methods for crystal plasticity simulations of heterogeneous materials. Int. J. Plast. (ISSN: 07496419) 66, 31–45. http://dx.doi.org/10.1016/j.ijplas.2014.02.006.

Thool, K., Patra, A., Fullwood, D., Krishna, K.V.M., Srivastava, D., Samajdar, I., 2020. The role of crystallographic orientations on heterogeneous deformation in a zirconium alloy: A combined experimental and modeling study. Int. J. Plast. (ISSN: 07496419) 133, http://dx.doi.org/10.1016/j.ijplas.2020.102785.

Voce, E., 1948. The relationship between stress and strain for homogeneous deformations. J. the Institute of Metals 74, 537–562.

Voigt, W., 1889. Ueber die beziehung zwischen den beiden Elasticitätsconstanten isotroper Körper. Ann. Phys. (ISSN: 15213889) 274 (12), 573–587. http://dx.doi.org/10.1002/andp.18892741206.

Voyiadjis, G.Z., Abed, F.H., 2005. Effect of dislocation density evolution on the thermomechanical response of metals with different crystal structures at low and high strain rates and temperatures. Archives of Mechanics (ISSN: 03732029) 57 (4), 299–343.

Wong, S.L., Madivala, Ma., Prahl, U., Roters, F., Raabe, D., 2016. Acta materialia A crystal plasticity model for twinning- and transformation-induced plasticity. Acta Mater. (ISSN: 1359-6454) 118, 140–151. http://dx.doi.org/10.1016/j.actamat.2016.07.032.

Yuan, S., Huang, M., Zhu, Y., Li, Z., 2018. A dislocation climb/glide coupled crystal plasticity constitutive model and its finite element implementation. Mech. Mater. (ISSN: 01676636) 118, 44–61. http://dx.doi.org/10.1016/j.mechmat.2017.12.009.

Yuan, S., Zhu, Y., Huang, M., Liang, S., Li, Z., 2020. Dislocation-density based crystal plasticity model with hydrogen-enhanced localized plasticity in polycrystalline face-centered cubic metals. Mech. Mater. (ISSN: 01676636) 148, http://dx.doi.org/10.1016/j.mechmat.2020.103472.

Yuan, S., Zhu, Y., Liang, S., Huang, M., Li, Z., 2019. Dislocation-density based size-dependent crystal plasticity framework accounting for climb of piled up dislocations at elevated temperature. Mech. Mater. (ISSN: 01676636) 134, http://dx.doi.org/10.1016/j.mechmat.2019.04.015.

Zhao, P., Song En Low, T., Wang, Y., Niezgoda, S.R., 2016. An integrated full-field model of concurrent plastic deformation and microstructure evolution: Application to 3D simulation of dynamic recrystallization in polycrystalline copper. Int. J. Plast. (ISSN: 07496419) 80, http://dx.doi.org/10.1016/j.ijplas.2015.12.010.

Zhao, P., Wang, Y., Niezgoda, S.R., 2018. Microstructural and micromechanical evolution during dynamic recrystallization. Int. J. Plast. (ISSN: 07496419) 100, http://dx.doi.org/10.1016/j.ijplas.2017.09.009.